

# Deciphering signatures of Kerr-Sen black holes in presence of plasma from the Event Horizon Telescope data

Siddharth Kumar Sahoo <sup>\*1</sup> and Indrani Banerjee <sup>†1</sup>

<sup>1</sup>Department of Physics and Astronomy, National Institute of Technology, Rourkela, Odisha-769008, India

## Abstract

The present work explores the role of the dilaton charge  $r_2$  and the plasma environment in explaining the observed images of M87\* and Sgr A\*. Dilaton charges are associated with Kerr-Sen black holes, the stationary, axi-symmetric black hole solution in the Einstein-Maxwell-dilaton-axion (EMDA) gravity which arise in the low energy effective action of superstring theories. We investigate the impact of the background spacetime (here dilaton charge and spin) and the plasma environment in modifying the shape and size of the black hole shadow. The theoretically derived shadow is compared with the observed images of M87\* and Sgr A\* which enables us to constrain the background spacetime in presence of the plasma environment. Our analysis reveals that the shadow of M87\* favors the Kerr scenario and rules out  $r_2 > 0.48$ , while the shadow of Sgr A\* exhibits a marginal preference towards the Kerr-Sen scenario (although GR is allowed within  $1-\sigma$ ) and rules out  $r_2 > 1$ . Thus, large values of dilaton charge are disfavored for M87\* and Sgr A\* and this result holds good irrespective of the inhomogeneous plasma environment. In fact, the presence of plasma further constrains the allowed parameter space of  $r_2$  and within the observed  $1-\sigma$  interval, the present data cannot distinguish between the Kerr and the Kerr-Sen black holes with mild dilaton charges. Moreover, the shadows of M87\* and Sgr A\* rule out very dense inhomogeneous plasma environments surrounding these objects and hence, black holes with less dense plasma environments seem to be good sites to detect signatures of dilaton charge. These findings not only underscore the importance of considering plasma effects in shadow related studies but also provide a pathway for refining constraints on alternative gravitational theories using black hole observations.

## 1 Introduction

The detection of gravitational waves [1–3] and the release of images of M87\* [4–9] and Sgr A\* [9–16] have demonstrated the success of general relativity (GR) in the strong field regime. These observations have also opened a window for strong field tests of GR (particularly with enhanced sensitivity in near future), where we expect to observe deviations from predictions of GR [17–20]. Detecting deviations from GR is important because, even if GR has passed many experimental tests, it still falls short in providing a complete understanding of gravity. The cosmological constant problem [21, 22], the accelerated expansion of the universe [23, 24], the presence of singularities in the theory [25–27] and its inconsistency with quantum theory [28] highlight the inadequacies of GR

---

<sup>\*</sup>521ph1007@nitrkl.ac.in

<sup>†</sup>banerjeein@nitrkl.ac.in

and the necessity for a more complete theory of gravity which can potentially address the above issues.

Black holes (BHs) are the most compact objects in the Universe and their extreme gravity makes them one of the ideal laboratories to test GR and alternative theories of gravity using astrophysical observations [20, 29]. Light from different sources, which also include radiation from the accretion disk surrounding a BH, are affected by its strong gravity before reaching the observer. Not all rays of light are able to escape the strong gravity of the black hole and reach the observer at infinity, thus the observer in general sees a dark region surrounded by a bright ring which corresponds to light rays which just succeed to escape the gravitational potential of the BH [30]. This dark region is called the black hole shadow and the bright ring is called the photon ring [30]. In many of the cases the light geodesics form spherical photon orbits [31] and the projection of these orbits on the observer's sky is called the *critical curve/boundary curve* [30, 32, 33] or more generally the shadow. The shadow of a Schwarzschild BH was first calculated by Synge [34] while Bardeen investigated the shadow of a Kerr BH for the first time [35]. Later, Synge's work was extended by incorporating a static and spherically symmetric plasma distribution [36] which followed studies on stationary, axi-symmetric plasma distributions in the Kerr spacetime [37].

In the present work we investigate the interplay between the string inspired Einstein-Maxwell-dilaton-axion (EMDA) gravity [38, 39] and the surrounding plasma environment in explaining the observed images of M87\* and Sgr A\*. EMDA gravity arises in the low energy effective action of heterotic string theory compactified on a  $6-d$  torus,  $T^6$ , giving rise to a pure  $N = 4$ ,  $d = 4$  supergravity coupled to  $N = 4$  super Yang-Mills theory, which results in a pure supergravity theory after appropriate truncation. The bosonic sector of this supergravity theory coupled to the  $U(1)$  gauge field corresponds to the EMDA gravity [38]. The Kerr-Sen solution in EMDA gravity represents the stationary axi-symmetric space time around a charged rotating black hole (BH) [39] which is characterized uniquely by three quantities, i. e.  $M$  (mass of BH),  $a$  (spin of BH), and  $r_2$  (dilaton charge). The dilaton charge stems from the electric charge and the dilaton field while the axion field imparts rotation to the Kerr-Sen BHs.

Astrophysical implications of Kerr-Sen BHs have been explored in the context of strong gravitational lensing and black hole shadows [40–46], continuum and reflection spectrum of black holes [47, 48], quasi-periodic oscillations [49] and jet power and radiative efficiency of microquasars [50]. In our previous work [46], we had obtained constraints on the dilaton charge using the observations of M87\* and Sgr A\* by EHT collaboration [4, 11]. The present work is a continuation of our previous work [46] where we revisit the constraints on the dilaton charge of M87\* and Sgr A\* by taking into account the effect of the surrounding plasma environment. This is important because astrophysical black holes are surrounded by an accretion disk containing plasma [37, 51], hence considering the effect of plasma on the shadow outline may provide more reasonable constraints on the background metric. Plasma is a dispersive medium and it affects light rays of different frequencies differently. While this effect may be insignificant for optical and higher frequencies, in the radio frequency domain its effect is expected to be more pronounced, particularly if the plasma density is high. Since, the EHT observes the shadows of M87\* and Sgr A\* in the radio frequency range [4–16], investigating the role of plasma on the observed shadows is important.

Investigating the impact of pressureless, non-magnetized plasma on radio signals began since the 1960s with the study of deflection of radio signals near the solar corona which can be approximated by a non-magnetized, pressureless plasma [52, 53]. Since BHs are surrounded by an accretion disk, it is important to investigate the impact of plasma on the radio signals reaching the earth from the vicinity of BHs. This motivated the study of light deflection in the Schwarzschild and Kerr spacetime

in pressureless, non-magnetized plasma environments [54] following which gravitational lensing was investigated with different methods in the presence of plasma [55–61]. This followed studies on the implications of plasma in the strong-bending regime (e.g. multiple imaging properties) [54, 56, 62] and other astrophysical observations [63–65]. Recent years have witnessed increasingly more interest in studies related to gravitational lensing [66–71] and shadows [72–77] in the presence of plasma.

In the present work we investigate the trajectories of light rays in the vicinity of Kerr-Sen BHs surrounded by a pressureless, non-magnetized plasma. We consider plasma distributions which ensure separability of the Hamilton-Jacobi equations leading to the presence of a generalized Carter constant [37, 76]. This in turn leads to first order geodesic equations for all the four coordinates and enables us to analytically obtain the shadow of Kerr-Sen BHs in the presence of plasma. These calculations hold good for any observer position and inclination [37, 78]. The theoretically obtained shadows are compared with the observed images of M87\* and Sgr A\* which enables us to establish constraints on the dilaton charge of these BHs and the surrounding plasma environment. The present work thus provides a framework to constrain the deviations from the Kerr scenario in the presence of plasma.

**Paper outline:** In Section 2 we give a brief overview of the EMDA gravity and discuss briefly about the Kerr Sen black hole. Section 3 summarizes the propagation of light rays in a stationary, axisymmetric spacetime in presence of a pressureless, non-magnetized plasma environment. Section 3.1 discusses the first order geodesic equations for photons moving in the Kerr-Sen spacetime in presence of non-magnetised, pressureless plasma while in Section 3.2 the expression of shadow outline considering an observer at a finite distance from the black hole is derived. In Section 4, we report the variation in the shadow of Kerr-Sen BHs with variation in the dilaton charge, spin, inclination and plasma environments. Section 5 outlines the methodology used to constrain the dilaton charge parameter in the presence of plasma from the EHT data and reports the constraints for M87\* (Section 5.1) and Sgr A\* (Section 5.2). We summarize the main findings and implications of our work in Section 6 and discuss some avenues which can be explored in future. We use geometrized units ( $G = c = 1$ ) and the metric signature is chosen to be  $(-, +, +, +)$ . However, during comparison with observations we convert back to SI units.

## 2 Einstein-Maxwell-dilaton-axion gravity

Einstein-Maxwell-dilaton-axion gravity is a string theory based alternate gravity model which roughly speaking results from the compactification of heterotic string theory to 4 dimensions and taking low energy limit of the effective action  $S$  [38, 39, 79, 80]. Along with the metric tensor and Maxwell field, the theory also contains dilaton and axion fields which are related to string theory. One of the interesting feature of EMDA gravity is, classical solutions in this theory can be used to investigate signatures of string theory as it still retains S and T dualities of string theory [38]. The action  $S$  of EMDA gravity is given as,

$$S = \frac{1}{16\pi} \int \sqrt{-g} d^4x (R - 2\partial_\mu \xi \partial^\mu \xi - \frac{1}{3} W_{\rho\sigma\delta} W^{\rho\sigma\delta} + e^{-2\xi} F_{\alpha\beta} F^{\alpha\beta}) \quad (1)$$

In Equation (1)  $g$  is the determinant of the metric tensor and  $R$  the Ricci scalar associated with the 4-dimensional metric tensor  $g_{\mu\nu}$ ,  $\xi$  represents the dilatonic field,  $F_{\mu\nu} = \nabla_\mu \mathcal{A}_\nu - \nabla_\nu \mathcal{A}_\mu$  is Maxwell

field strength tensor and  $W_{\rho\sigma\delta}$  is the Kalb-Ramond field strength tensor [38, 39]. In four dimensions the Kalb-Ramond field strength tensor  $W_{\rho\sigma\delta}$  can be written in terms of the pseudo-scalar axion field  $\Lambda$  [38, 81], such that,

$$W_{\alpha\beta\delta} = \frac{1}{2}e^{4\xi}\epsilon_{\alpha\beta\delta\gamma}\partial^\gamma\Lambda \quad (2)$$

The action in Equation (1) written in terms of the axion field assumes [38] the form,

$$S = \frac{1}{16\pi} \int \sqrt{-g} d^4x \left[ R - 2\partial_\nu\xi\partial^\nu\xi - \frac{1}{2}e^{4\xi}\partial_\nu\Lambda\partial^\nu\Lambda + e^{-2\xi}F_{\rho\sigma}F^{\rho\sigma} + \Lambda F_{\rho\sigma}\tilde{F}^{\rho\sigma} \right] \quad (3)$$

The equations of motion for the axion  $\Lambda$ , dilaton  $\xi$  and the vector potential  $\mathcal{A}_\mu$  can be obtained by varying the action  $S$  with respect to the corresponding fields. The field equations for gravity in EMDA theory can be obtained by varying the action in Equation (3) with respect to  $g_{\mu\nu}$ . The modified Einstein equations take the form

$$G_{\mu\nu} = \mathcal{T}_{\mu\nu}(F, \xi, \Lambda) \quad (4)$$

and

$$\begin{aligned} \mathcal{T}_{\mu\nu}(F, \xi, \Lambda) = & e^{2\xi}(4F_{\mu\rho}F_\nu^\rho - g_{\mu\nu}F^2) - g_{\mu\nu}(2\partial_\gamma\xi\partial^\gamma\xi + \frac{1}{2}e^{4\xi}\partial_\gamma\Lambda\partial^\gamma\Lambda) \\ & + \partial_\mu\xi\partial_\nu\xi + e^{4\xi}\partial_\mu\Lambda\partial_\nu\Lambda \end{aligned} \quad (5)$$

In Equation (4) and Equation (5),  $\mathcal{T}_{\mu\nu}$  is the energy-momentum tensor and  $G_{\mu\nu}$  is the Einstein tensor. The stationary, axisymmetric, charged, rotating black hole solution of Equation (4) in EMDA gravity is the Kerr Sen solution [39, 81]. The form of the metric in Boyer-Lindquist coordinates  $(t, r, \theta, \phi)$  [82] is given by,

$$ds^2 = -\left(1 - \frac{2Mr}{\rho}\right) dt^2 + \frac{\rho}{\Delta} dr^2 + \rho d\theta^2 + \frac{\sin^2\theta}{\rho} [(r+r_2)r + a^2]^2 - \Delta a^2 \sin^2\theta d\phi^2 - \frac{4aMr}{\rho} dt d\phi \quad (6)$$

where

$$\rho = r(r+r_2) + a^2 \cos^2\theta \quad (7)$$

$$\Delta = r(r+r_2) + a^2 - 2Mr \quad (8)$$

The dilaton charge parameter  $r_2 = \frac{q^2 e^{2\xi_0}}{M}$  is related to the electric charge of the black hole  $q$ , and the asymptotic value of the dilaton field  $\xi$ . The expression of  $r_2$  indicates  $r_2 \geq 0$ . The event horizon of the Kerr Sen black hole can be obtained by solving the equation  $g^{rr} = 0$ , which gives us

$$\frac{r_{h\pm}}{M} = \left(1 - \frac{r_2}{2M} \pm \sqrt{\left(1 - \frac{r_2}{2M}\right)^2 - \frac{a^2}{M^2}}\right) \quad (9)$$

In above equation  $r_{h-}$  and  $r_{h+}$  represent the inner and outer horizons of the black hole respectively. Imposing the condition of black hole having real, positive event horizon, we obtain two restrictions. First, the upper bound of dilaton charge parameter  $\frac{r_{2max}}{M} = 2$ . Second, the maximum spin  $a_{max}$  for a Kerr Sen black hole is  $\frac{a_{max}}{M} = \left(1 - \frac{r_2}{2M}\right)$  for a given  $r_2$ . In what follows we will scale all distances with  $M$  such that  $r \equiv \frac{r}{M}$  and  $r_2 \equiv \frac{r_2}{M}$ .

### 3 Overview of light rays in a plasma in stationary axisymmetric spacetime

As discussed in the previous section, the Kerr-Sen spacetime is a stationary, axisymmetric spacetime admitting Killing vectors  $\partial_t$  and  $\partial_\phi$ . For purposes specific to our work, we consider plasma in a stationary, axisymmetric spacetime with metric tensor  $g_{\mu\nu}(r, \theta)$ . The plasma frequency  $\omega_P(x^\mu)$  is related to the electron number density  $\mathcal{N}(x^\mu)$  by the relation

$$\omega_P^2(x^\mu) = \frac{4\pi e^2}{m_e} \mathcal{N}(x^\mu) \quad (10)$$

In above equation  $e$  and  $m_e$  are the charge and mass of electron, respectively. The path of the light rays in the plasma can be determined using Hamiltonian formalism. For our work we consider pressureless, non-magnetised plasma where the Hamiltonian  $\mathcal{H}$  for light ray is given by [32, 83, 84]

$$\mathcal{H}(x^\mu, p^\mu) = \frac{1}{2} (g^{\mu\nu} p_\mu p_\nu + \omega_P(x^\mu)^2) \quad (11)$$

and relations for obtaining  $\dot{x}^\mu$  and  $p^\mu$  from  $\mathcal{H}$  are given by

$$\dot{x}_\mu = \frac{\partial \mathcal{H}}{\partial p^\mu} \quad (12)$$

$$\dot{p}_\mu = -\frac{\partial \mathcal{H}}{\partial x^\mu} \quad (13)$$

The dot on  $x^\mu$  and  $p^\mu$  represents derivative with respect to some curve parameter  $\lambda$ . This implies  $p_t$  and  $p_\phi$  are the constants of motion. Let  $\omega(x) \equiv \omega(r, \theta)$  represent the frequency of light at  $(r, \theta)$ . We decompose the momentum  $p^\mu$  of the light ray in a direction parallel and orthogonal to a timelike observer with normalized four-velocity  $u^\mu$ , i. e.,  $u_\mu u^\mu = -1$  in the curved spacetime. Thus we decompose  $p^\mu$  as

$$p^\mu = \omega(x) u^\mu + k^\mu \quad (14)$$

In the above equation the first and second terms represent components of  $p^\mu$  parallel and orthogonal to  $u^\mu$  respectively. The frequency of the light ray can be written as

$$\omega(x) = -p_\mu u^\mu \quad (15)$$

while

$$k^\mu = p^\mu + p_\nu u^\nu u^\mu \quad (16)$$

Substituting Equation (14) in Equation (11) and using the property  $\mathcal{H} = 0$  for photons or light rays, we get

$$\omega(x)^2 = k^\mu k_\mu + \omega_P^2(x) \quad (17)$$

Due to spacelike nature of  $k^\mu$ , it follows

$$\omega^2(x) \geq \omega_P^2(x) \quad (18)$$

The above inequality is the condition for light propagation in a plasma. This means light propagation in a region of plasma is possible as long as the inequality Equation (18) is satisfied. The

above condition Equation (18) can also be interpreted in terms of the refractive index  $\mathbf{n}(r, \theta)$ . We first define the phase velocity of the light wave  $v_p$  and the index of refraction  $\mathbf{n}$  as,

$$v_p(r, \theta) = \left( \frac{\omega^2(r, \theta)}{k_\mu(r, \theta)k^\mu(r, \theta)} \right)^{\frac{1}{2}} \quad (19)$$

$$\mathbf{n}(r, \theta) = \frac{1}{v_p(r, \theta)} \quad (20)$$

since  $c = 1$ . Using Equation (17) and Equation (19) in Equation (20) we get

$$\mathbf{n} = \sqrt{1 - \frac{\omega_P^2(x)}{\omega^2(x)}} \quad (21)$$

Thus light propagation condition in Equation (18) translates to  $\mathbf{n}(r, \theta) \geq 0$  [37, 85]. For a static timelike observer  $u^\mu = \frac{\delta_t^\mu}{\sqrt{-g_{tt}}}$ , the frequency of light  $\omega(r, \theta) \equiv \omega(x)$  measured at location  $(r, \theta)$  and  $\omega_0$  are related by [37]

$$\omega(x) = \frac{\omega_0}{\sqrt{-g_{tt}}} \quad (22)$$

Thus,  $\omega_0$  corresponds to the frequency of light measured by an observer at rest at infinity.

### 3.1 Motion of photons in plasma in Kerr Sen spacetime

In this section, we will obtain the equations of geodesics traced by light rays in presence of plasma around a Kerr-Sen black hole. We consider the plasma as a dispersive medium, i.e, the presence of plasma modifies the refractive index of the surrounding space time, through which the light rays travel, hence affecting the path of the light rays.

Substituting the components of Kerr Sen metric in the Hamiltonian Equation (11) and simplifying we get

$$\mathcal{H} = \frac{1}{2\rho} \left( \left( \frac{p_\phi}{\sin \theta} + a \sin \theta p_t \right)^2 - \frac{1}{\Delta} (ap_\phi + p_t(a^2 + r(r + r_2)))^2 + p_\theta^2 + \Delta p_r^2 + \rho \omega_P^2 \right) = 0 \quad (23)$$

From the Hamilton-Jacobi equation we have

$$\mathcal{H} + \frac{\partial \mathcal{S}(t, r, \theta, \phi)}{\partial \lambda} = 0 \quad (24)$$

where

$$p_\mu = \frac{\partial \mathcal{S}}{\partial x^\mu} \quad (25)$$

We note that for light rays in plasma in Equation (11)  $\mathcal{H} = 0$  which yields  $\frac{\partial \mathcal{S}}{\partial \lambda} = 0$ . Taking action  $\mathcal{S}$  of the form

$$\mathcal{S} = p_t t + S_r(r) + S_\theta(\theta) + p_\phi \phi \quad (26)$$

and substituting in Equation (25) and Equation (26) in Equation (23) we get,

$$\left(\frac{p_\phi}{\sin \theta} + a \sin \theta p_t\right)^2 - \frac{1}{\Delta} (ap_\phi + p_t(a^2 + r(r + r_2)))^2 + \Delta \left(\frac{d\mathcal{S}_r(r)}{dr}\right)^2 + \left(\frac{d\mathcal{S}_\theta(\theta)}{d\theta}\right)^2 + \rho \omega_P(r, \theta)^2 = 0 \quad (27)$$

In the presence of plasma, the separability of the  $r$  and  $\theta$  dependent part of the above equation holds true *iff* the quantity  $\omega_P(r, \theta)^2$  has a form like

$$\omega_P(r, \theta)^2 = \frac{f(r) + g(\theta)}{\rho} \quad (28)$$

where,  $f(r)$  and  $g(\theta)$  are functions of  $r$  and  $\theta$  respectively. The separability condition for  $r_2 = 0$  (Kerr metric case) was first obtained in [37], for a more general result refer [76]. From the condition of light propagation in plasma ( $\omega(r, \theta)^2 \geq \omega_P(r, \theta)^2$ ) we infer that, in order for light to propagate from the source to observer in the plasma medium, the plasma frequency function can not be unbounded.

Thus, Hamiltonian Equation (23) can be written in the form

$$\left(\frac{p_\phi}{\sin \theta} + a \sin \theta p_t\right)^2 + g(\theta) + \left(\frac{d\mathcal{S}_\theta(\theta)}{d\theta}\right)^2 = \frac{1}{\Delta} (ap_\phi + p_t(a^2 + r(r + r_2)))^2 - \Delta \left(\frac{d\mathcal{S}_r(r)}{dr}\right)^2 - \Delta f(r) \quad (29)$$

As the left hand side of the equation depends on  $\theta$  and the right hand side depends on  $r$ , thus, both expressions must be equal to a constant. We represent the constant by the symbol  $\mathcal{C}$ . The constant of separability  $\mathcal{C}$  is called the generalised Carter constant [37, 86]. As  $p_r = \frac{d\mathcal{S}_r(r)}{dr}$  and  $p_\theta = \frac{d\mathcal{S}_\theta(\theta)}{d\theta}$ , we obtain

$$\Delta^2 p_r^2 = (ap_\phi + p_t(a^2 + r(r + r_2)))^2 - \Delta f(r) - \mathcal{C} \Delta \quad (30)$$

$$p_\theta^2 = \mathcal{C} - \left(\frac{p_\phi}{\sin \theta} + a \sin \theta p_t\right)^2 - g(\theta) \quad (31)$$

The equations of geodesics of light and refractive index in presence of plasma in the Kerr Sen space-time are as follows:

$$\frac{\rho^2 \dot{r}^2}{\omega_0^2} = (-a\eta + (a^2 + r(r + r_2)))^2 - \Delta f(r) - \mathcal{Q} \Delta = K(r) \quad (32)$$

$$\frac{\rho^2 \dot{\theta}^2}{\omega_0^2} = \mathcal{Q} - \left(-a \sin \theta + \frac{\eta}{\sin \theta}\right)^2 - g(\theta) = J(\theta) \quad (33)$$

$$\frac{\rho \dot{\phi}}{\omega_0} = \frac{(\rho - 2r)\eta - 2ar \sin^2 \theta}{\Delta \sin^2 \theta} \quad (34)$$

$$\frac{\rho \dot{t}}{\omega_0} = \frac{-(\Delta a^2 \sin^2 \theta - ((r + r_2)r + a^2)^2) - 2ra\eta}{\Delta} \quad (35)$$

The variation of refractive index  $n$  of plasma now becomes

$$n^2(r, \theta) = 1 - \frac{f(r) + g(\theta)}{\omega(r, \theta)^2 \rho} \quad (36)$$

In above equations  $\mathcal{Q} = \frac{c}{\omega_0^2}$  and  $\eta = \frac{p_\phi}{\omega_0}$  (where  $\omega_0 = -p_t$ ). Equation (32), Equation (33), Equation (34) and Equation (35) when solved, gives the path of the light rays traveled in a plasma medium. The effect of plasma on light ray geodesics is taken into account with presence of  $f(r)$  and  $g(\theta)$  in the geodesic equations.

Similar to Kerr black hole, light rays can form spherical photon orbits in the Kerr-Sen spacetime as well [31, 46, 87], the projection of these spherical photon orbits on the observer's sky gives the *boundary curve* or *critical curve* (also generally referred as shadow outline). We want to take into account the effect of plasma on shadow outline which will be a more general and astrophysically relevant study. In order to find the equation of the shadow outline which is the projection of the spherical photon orbits, we have to first obtain the condition of spherical photon orbits, which corresponds to  $\dot{r} = 0$  and  $\ddot{r} = 0$ , which means  $K(r_p) = 0$  and  $K'(r_p) = 0$ , where  $r_p$  represents the radius of the spherical photon orbit. From Equation (32) and Equation (33),

$$K(r) = (-a\eta + (a^2 + r(r + r_2)))^2 - \Delta f(r) - \mathcal{Q} \Delta \quad (37)$$

$$J(\theta) = \mathcal{Q} - \left(-a \sin \theta + \frac{\eta}{\sin \theta}\right)^2 - g(\theta) \quad (38)$$

The condition of spherical photon orbits when imposed on the radial geodesic equation, gives expression for allowed values of constants of motion  $\mathcal{Q}$  and  $\eta$  for a given spherical photon orbit of radius  $r_p$ . For the light ray geodesics of Kerr Sen black hole surrounded by plasma [37] we obtain the expressions of  $\mathcal{Q}$  and  $\eta$  as:

$$\eta(r_p) = -\frac{1}{a\Delta'} \left( 2(a^2 - r_p^2) \pm (2r_p + r_2)\Delta \sqrt{1 - \frac{f'(r_p)\Delta'}{(2r_p + r_2)^2}} \right) \quad (39)$$

$$\mathcal{Q}(r_p) = \frac{\Delta(2r_p + r_2)^2}{\Delta'^2} \left( 1 \pm \sqrt{1 - \frac{f'(r_p)\Delta'}{(2r_p + r_2)^2}} \right)^2 - f(r_p) \quad (40)$$

An additional condition which needs to be imposed is  $J(\theta) \equiv \dot{\theta}^2 \geq 0$ , which gives us

$$\mathcal{Q}(r_p) - \left(-a \sin \theta + \frac{\eta(r_p)}{\sin \theta}\right)^2 - g(\theta) \geq 0 \quad (41)$$



or

$$\mathcal{Q}(r_p)a^2\sin^2\theta - (-a\eta(r_p) + a^2\sin^2\theta)^2 \geq a^2\sin^2\theta g(\theta) \quad (42)$$

When Equations (39) and (40) are substituted in Equation (41) or Equation (42), the values of  $r_p$  that satisfy the condition give the allowed values of radius of photon orbits (the spherical photon region). The stability of spherical photon orbits are inferred by analysis of  $K''(r)$  given by

$$K''(r) = 4(a^2 - a\eta + r(r + r_2)) - \Delta f''(r) - 2f'(r)\Delta' - f(r)\Delta'' - Q\Delta'' + 2(2r + r_2)^2 \quad (43)$$

For unstable photon orbits  $K''(r_p) > 0$  needs to be satisfied.

### 3.2 Obtaining the shadow outline

In order to obtain the equation of the shadow outline, we follow the procedure as explained in [37, 88, 89]. We consider an observer at a distance  $d$  and at an angle of inclination  $\theta_i$ . We associate the following ortho-normal tetrads to the observer at  $(d, \theta_i)$ :

$$e_0^\mu = \frac{1}{\sqrt{\rho\Delta}} \{r(r + r_2) + a^2, 0, 0, a\} \Big|_{(d, \theta_i)} \quad (44)$$

$$e_1^\mu = \frac{1}{\sqrt{\rho}} \{0, 0, 1, 0\} \Big|_{(d, \theta_i)} \quad (45)$$

$$e_2^\mu = \frac{-1}{\sqrt{\rho}\sin\theta} \{a\sin^2\theta, 0, 0, 1\} \Big|_{(d, \theta_i)} \quad (46)$$

$$e_3^\mu = -\sqrt{\frac{\Delta}{\rho}} \{0, 1, 0, 0\} \Big|_{(d, \theta_i)} \quad (47)$$

Here,  $e_0^\mu$  is the 4-velocity of the observer. The tangent vector to the light ray geodesic emanating from the observer position  $(d, \theta_i)$  is,

$$\dot{\Gamma}^\mu(\lambda) = \dot{t}\partial_t + \dot{r}\partial_r + \dot{\theta}\partial_\theta + \dot{\phi}\partial_\phi \quad (48)$$

where overdot implies derivative with respect to a curve parameter  $\lambda$ . At the location of the observer the tangent vector can be expanded in the basis of orthonormal tetrads given by Equation (44) - Equation (47),

$$\dot{\Gamma}^\mu(\lambda) = -\Upsilon e_0^\mu + \beta(\sin\gamma\cos\delta e_1^\mu + \cos\gamma\cos\delta e_2^\mu + \cos\gamma e_3^\mu) \quad (49)$$

Here  $\Upsilon$  and  $\beta$  are positive factors. From Hamilton's equations Equation (12) and Equation (13) we have  $\dot{x}^\mu = p^\mu$ . Using the result  $g_{\mu\nu}\dot{\Gamma}^\mu\dot{\Gamma}^\nu = -\omega_P^2$ , we obtain the relation between  $\Upsilon$  and  $\beta$  as:

$$\Upsilon^2 - \beta^2 = \omega_P^2(d, \theta_i) \quad (50)$$

By projecting  $\dot{\Gamma}^\mu$  as given in Equation (48) and Equation (49) along  $e_0^\mu$ , and comparing both results we can obtain  $\Upsilon$ .

$$\Upsilon = g_{\mu\nu} \dot{\Gamma}^\mu e_0^\nu = -\frac{(r+r_2)r+a^2}{\sqrt{\rho\Delta}} + \frac{a\eta}{\sqrt{\rho\Delta}} \quad (51)$$

Substituting the expression of  $\Upsilon$  in Equation (50) one can obtain the expression of  $\beta$ .

$$\beta = \sqrt{\frac{(a\eta - (r(r+r_2)+a^2))^2 - \Delta(f(r)+g(\theta))}{\rho\Delta}} \quad (52)$$

By equating the coefficients of  $\partial_r$  and  $\partial_\phi$  in Equation (48) and Equation (49) we can obtain the expressions of  $\gamma$  and  $\delta$ , respectively. Equating coefficients of  $\partial_r$  we get

$$-\beta \cos \gamma \sqrt{\frac{\Delta}{\rho}} = \dot{r} \quad (53)$$

Using radial geodesic equation Equation (32) in Equation (53) one obtains,

$$\sin \gamma = \sqrt{\frac{(\mathcal{Q} - g(\theta))\Delta}{(a\eta(r_p) - (r(r+r_2)+a^2))^2 - \Delta(f(r)+g(\theta))}} \quad (54)$$

Similarly, for the case of  $\partial_\phi$  we get

$$\dot{\phi} = \frac{-a\Upsilon}{\sqrt{\rho\Delta}} - \frac{\beta \sin \gamma \sin \delta}{\sin \theta \sqrt{\rho}} \quad (55)$$

Using Equation (34) one obtains,

$$\sin \delta = \frac{-\eta + a \sin^2 \theta}{\sin \theta \sqrt{\mathcal{Q} - g(\theta)}} \Big|_{(d, \theta_i)} \quad (56)$$

For the observer, the local coordinates  $(\gamma, \delta)$  should be calculated at  $(d, \theta_i)$ , such that

$$\sin \gamma = \sqrt{\frac{(\mathcal{Q} - g(\theta))\Delta}{(a\eta - (r(r+r_2)+a^2))^2 - \Delta(f(r)+g(\theta))}} \Big|_{(d, \theta_i)} \quad (57)$$

$$\sin \delta = \frac{-\eta + a \sin^2 \theta}{\sin \theta \sqrt{\mathcal{Q} - g(\theta)}} \Big|_{(d, \theta_i)} \quad (58)$$

The shadow outline is the locus of all points in the observer's sky which when traced back along the light ray geodesic paths will reach the spherical photon orbits [37]. For a spherical photon radius  $r_p$  one needs to calculate the constants of motion  $\mathcal{Q}(r_p)$  and  $\eta(r_p)$  using Equation (40) and Equation (39). Then using Equation (57) and Equation (58) one calculates the angles  $\gamma$  and  $\delta$  which are angular coordinates of the shadow outline in the observer's celestial sphere. The range

of radius of photon orbits which should be used to plot the shadow are obtained by the following condition

$$\sin \delta(r_{p_{min/max}}) = \pm 1 \quad (59)$$

which can be written as

$$\frac{-\eta(r_p) + a \sin^2 \theta_i}{\sin \theta_i \sqrt{\mathcal{Q} - g(\theta_i)}} = \pm 1 \quad (60)$$

The above conditions mean that the shadow outline for the observer at  $(d, \theta_i)$  is contributed by the photon region which has turning points at  $\theta_i$ , i.e.  $J(\theta_i) = 0$ . For each value of  $r_p$  between  $r_{p_{min}}$  and  $r_{p_{max}}$  there is a unique  $\gamma$  given by Equation (57) but two values of  $\delta$  between  $(-\pi/2, \pi/2)$  and  $(\pi/2, 3\pi/2)$ . In order to obtain the  $x$  and  $y$  coordinates of the shadow we use the stereographic projection of the celestial sphere onto the plane tangent to the celestial sphere at  $\gamma = 0$ . This gives

$$x(r_p) = -2d \tan \left( \frac{\gamma(r_p)}{2} \right) \sin \delta(r_p) \quad (61)$$

$$y(r_p) = -2d \tan \left( \frac{\gamma(r_p)}{2} \right) \cos \delta(r_p) \quad (62)$$

the angular coordinate along the  $x$  and  $y$  axes are given by  $X = \frac{x}{d}$  and  $Y = \frac{y}{d}$  [33, 88]. The expressions of angular coordinates are

$$X(r_p) = -2 \tan \left( \frac{\gamma(r_p)}{2} \right) \sin \delta(r_p) \quad (63)$$

$$Y(r_p) = -2 \tan \left( \frac{\gamma(r_p)}{2} \right) \cos \delta(r_p) \quad (64)$$

In the equations Equation (63), Equation (64),  $X(r_p)$  and  $Y(r_p)$  are in the units of radian and thus can be used directly to calculate the angular diameter of the shadow outline. From the equations it can be shown that the shadow outline will be symmetric about the horizontal axis. The present approach also takes in consideration the effect of finite distance of the observer from the black hole in presence of plasma.

Thus, if  $r_{p_1}$  represents the radius of the spherical photon orbit corresponding to maximum angular height of the shadow from the horizontal, i.e.  $Y_{max} = Y(r_{p_1})$ , then the vertical angular diameter  $\Delta\Theta$  of the shadow can be computed using the formula given below:

$$\Delta\Theta = 2Y_{max} \quad (65)$$

In order to find  $r_{p_1}$  we solve the following equation,

$$\left. \frac{dY(r_p)}{dr_p} \right|_{(r_p=r_{p_1})} = 0 \quad (66)$$

where  $r_{p_{min}} < r_{p_1} < r_{p_{max}}$ . In case of a non-rotating black hole we obtain  $r_{p_1} = r_s$ , where  $r_s$  can be obtained by solving :

$$-\frac{1}{\Delta'} \left( 2(a^2 - r_p^2) \pm (2r_p + r_2)\Delta \sqrt{1 - \frac{f'(r_p)\Delta'}{\Delta'^2}} \right) = 0 \quad (67)$$

The above equation results from the fact that for non-rotating black hole,  $a\eta(r_p) = 0$  (see Equation (39)).

## 4 Shadow of Kerr-Sen black hole surrounded by plasma

In this section we study the nature of shadow of Kerr Sen black hole surrounded by a pressureless, non-magnetized plasma. We have already derived the  $X$  and  $Y$  coordinates of the shadow in the previous section. In order to proceed further one needs to specify the plasma profile. Recall, in Section 3.1 we obtained in Equation (28)

$$\omega_P(r, \theta)^2 = \omega_b^2 \left( \frac{f(r) + g(\theta)}{\rho} \right) \quad (68)$$

While using Equation (22) for the Kerr-Sen black hole,

$$\frac{\omega^2(x)}{\omega_0^2} = \left( 1 - \frac{2r}{\rho} \right)^{-1} \quad (69)$$

Using the condition Equation (18) we get,

$$\left( 1 - \frac{2r}{\rho} \right)^{-1} \geq \alpha \left( \frac{f(r) + g(\theta)}{\rho} \right) \quad (70)$$

where  $\alpha = \frac{\omega_b^2}{\omega_0^2}$ . On rearranging the above inequality we obtain

$$\alpha \leq \left( 1 - \frac{2r}{\rho} \right)^{-1} \left( \frac{f(r) + g(\theta)}{\rho} \right)^{-1} = F(r, \theta) \quad (71)$$

Thus, for a given plasma profile surrounding a Kerr Sen black hole of dilaton charge  $r_2$  and spin  $a$ , the maximum possible bound on  $\alpha$  is

$$\alpha_{max} = \left( 1 - \frac{2r}{\rho} \right)^{-1} \left( \frac{f(r) + g(\theta)}{\rho} \right)^{-1} \Big|_{min} \quad (72)$$

In our work, we will consider three plasma profiles satisfying the separability condition Equation (68) [37]:

$$\text{Profile 1: } \omega_P^2(r, \theta) = \alpha_1 \left( \frac{\sqrt{r}}{\rho} \right) \text{ here } f(r) = \sqrt{r} \text{ and } g(\theta) = 0 \quad (73)$$

$$\text{Profile 2: } \omega_P^2(r, \theta) = \alpha_2 \left( \frac{(1 + 2 \sin^2 \theta)}{\rho} \right) \text{ here } f(r) = 0 \text{ and } g(\theta) = (1 + 2 \sin^2 \theta) \quad (74)$$

$$\text{Profile 3: } \omega_P^2(r, \theta) = \alpha_3 \left( \frac{r(r + r_2) + a^2 \cos^2 \theta}{\rho} \right) \text{ here } f(r) = r(r + r_2) \text{ and } g(\theta) = a^2 \cos^2 \theta \quad (75)$$

#### 4.1 Variation of shadow considering profile 1

The plasma profile in Equation (73) was considered by Shapiro [90] when he studied steady-state spherical accretion of interstellar gas/plasma onto Kerr black holes. The plasma is assumed to be at rest at infinity, but close to the black hole it acquires an angular momentum due to the black hole's rotation, i.e., at  $r \gg r_g$  the accreting fluid only has radial velocity. This is a reasonable approximation to model the geometrically thick and optically thin accretion flow generally prevalent in supermassive black holes accreting from the surrounding ISM, e.g. Sgr A\*. The velocity of the plasma in the regime  $r_{h+} < r < r_c$  (where the plasma density through which the photon travels is substantial) is comparable to the free-fall velocity  $u_r = \sqrt{2GM/r}$ , where  $r_{h+}$  is the outer horizon and  $r_c = GM/c_s^2$  is the capture radius,  $c_s$  being the sound speed [90]. Considering conservation of mass and energy-momentum tensor, it can be shown that

$$4\pi n u_r \rho = A = \text{constant} \quad (76)$$

which in turn implies

$$n = \frac{C_0 \sqrt{r}}{\rho} \quad (77)$$

which is the plasma profile considered in this section. Here,  $n$  is the density of the plasma measured in the comoving frame.

In profile 1, the plasma parameter  $\alpha_1 \geq 0$  because  $\omega_P^2 \geq 0$ . Furthermore,  $\alpha_1$  cannot take arbitrary high values because the condition (71) needs to be satisfied for light propagation in plasma. The maximum value of  $\alpha_1$  is determined by condition (72). We denote  $F(r, \theta)$  by  $F_1(r, \theta)$  for profile 1. In Figure 1 we plot the variation of  $F_1(r, \theta)$  with  $r$  at  $\theta = \frac{\pi}{6}$  (Red) and  $\frac{\pi}{2}$  (Blue). Figures 1a to 1c represent plots for  $r_2 = 0, 0.75$  and  $1.5$ , respectively. Furthermore, for each  $\theta$  and  $r_2$  we make plots for spins  $a = 0.1$  (Solid),  $0.5(1 - \frac{r_2}{2})$  (Dashed) and  $(0.999 - \frac{r_2}{2})$  (Dotted).

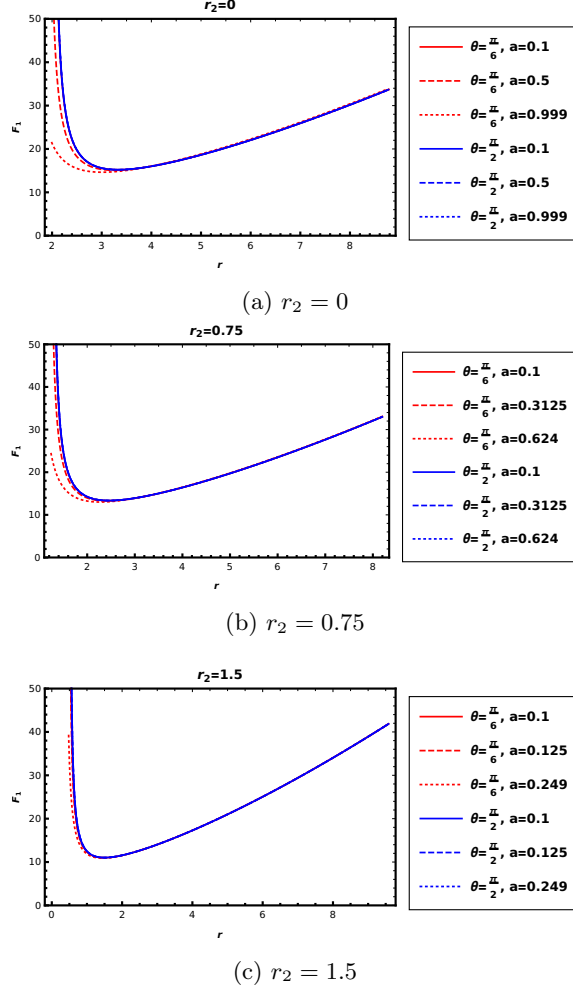


Figure 1: Variation of  $F_1(r, \theta)$  with  $r$  (in units of  $M$ ) at  $a = 0.1, 0.5(1 - \frac{r_2}{2})$  and  $0.999 - \frac{r_2}{2}$  for  $\theta = \frac{\pi}{6}$  (Red) and  $\frac{\pi}{2}$  (Blue) for different  $r_2$

From Figures 1a to 1c we make the following observations:

- For each choice of  $a$  and  $\theta$  for a given  $r_2$  in Figures 1a to 1c there exists a minimum.
- $F_1(r, \theta)$  is sensitive to  $a$  at lower values of  $\theta$ , and close to the black hole.
- $F_1(r, \theta)$  for a given  $r_2$  and  $a$  is nearly insensitive to the variation in  $\theta$  as we go away from the horizon.
- The minimum of  $F_1(r, \theta)$  (which corresponds to  $\alpha_{1max}$ ) in Figures 1a to 1c, decreases with an increase in  $r_2$ .
- The minimum value of  $F_1(r, \theta)$  can be used to estimate the maximum value of  $\alpha_1$  for a given  $r_2$ , that is, for  $r_2 = 0, 0.75$  and  $1.5$  the corresponding  $\alpha_{1max} \approx 16, 14$  and  $10$ , respectively.

We now study the effect of the dilaton charge, the spin of black hole, and the plasma parameter  $\alpha_1$  on the shadow at different inclination angles. We describe the necessary details about our study below :

- Figures 2 to 4 plots the variation of shadow with  $\alpha_1$  for different values of  $r_2$  and  $a$  assuming  $\theta_i = 15^\circ, 45^\circ$  and  $90^\circ$ , respectively.
- All the plots are done assuming a black hole of mass  $M = 6.2 \times 10^9 M_\odot$  and seen by an observer at a distance  $D \approx 5.6 \times 10^{10} M$  (or 16.8 Mpc), which correspond to mass and distance measurements of M87\* [4], respectively.
- Each column in Figures 2 to 4 is associated with a fixed  $r_2$ . Column 1 corresponds to  $r_2 = 0$ , column 2 corresponds to  $r_2 = 0.75$  and column 3 corresponds to  $r_2 = 1.5$ .
- Each column contains three plots for the chosen  $r_2$  with spins  $a = 0$ , half maximal spin  $a = 0.5 (1 - \frac{r_2}{2})$  and near maximal spin  $a = (0.999 - \frac{r_2}{2})$  as we go vertically downwards.
- In each sub figure the individual plots show shadow outlines for  $\alpha_1 = 0$  (Magenta curve),  $\alpha_1 = 5$  (Blue curve) and  $\alpha_1 = 10$  (Red curve) for a given  $r_2$ ,  $a$  and  $\theta_i$ . The  $X$  and  $Y$  angular coordinates are in units of  $\mu as$ , while the spin  $a$  and the dilaton charge  $r_2$  are in geometrised units.

From Figure 2 we draw the following conclusions:

- The contraction of the shadow size due to the dilaton charge  $r_2$  can be seen from the Figures 2a to 2c for all values of  $\alpha_1$ , i.e,  $\alpha_1 = 0$ ,  $\alpha_1 = 5$  and  $\alpha_1 = 10$ , which was also reported in [46]. This contraction due to  $r_2$  can also be seen in case of non-zero  $a$  and  $\alpha_1 = 0, 5$  and  $10$  as we go horizontally from Figures 2d to 2f and then from Figures 2e to 2g. Thus we observe contraction of shadow size due to  $r_2$  both in absence and presence of plasma and irrespective of the spin  $a$ .
- Figure 2a shows purely the effect of  $\alpha_1$  on the shadow size since  $r_2 = 0$  and  $a = 0$  at  $\theta = 15^\circ$ . We observe that as  $\alpha_1$  increases, the size of the shadow decreases. This effect of  $\alpha_1$  is quite generic irrespective of the choice of  $r_2$  and  $a$ . We also observe from Figures 2b to 2i that with non-zero dilaton charge  $r_2$  the shadow size decreases more strongly with increase in  $\alpha_1$ .
- The effect of spin  $a$  on shadow outline can be seen for given  $(r_2, \alpha_1, \theta_i)$  if we go vertically downwards along each column in Figure 2. In each column  $r_2$  and  $\theta_i$  are fixed. Comparing same colored shadow outline plots (which means same  $\alpha_1$ ), we observe that as spin  $a$  increases there is change of geometric center of the shadow.
- Note that all shadow outlines in Figure 2 are nearly circular. This is because of the small angle inclination  $\theta_i = 15^\circ$ .

We next consider shadow plots in Figure 3. From analysis of Figure 3 we draw the following conclusions:

- The increase in the dilaton charge  $r_2$  causes a contraction in the shadow size (Figures 3a to 3c), as was observed in the case of  $\theta_i = 15^\circ$  (see Figure 2). Interestingly, even though  $\theta_i$  has changed from  $15^\circ$  to  $45^\circ$ , the degree of contraction in vertical angular width of shadow due to  $r_2$  are nearly the same.

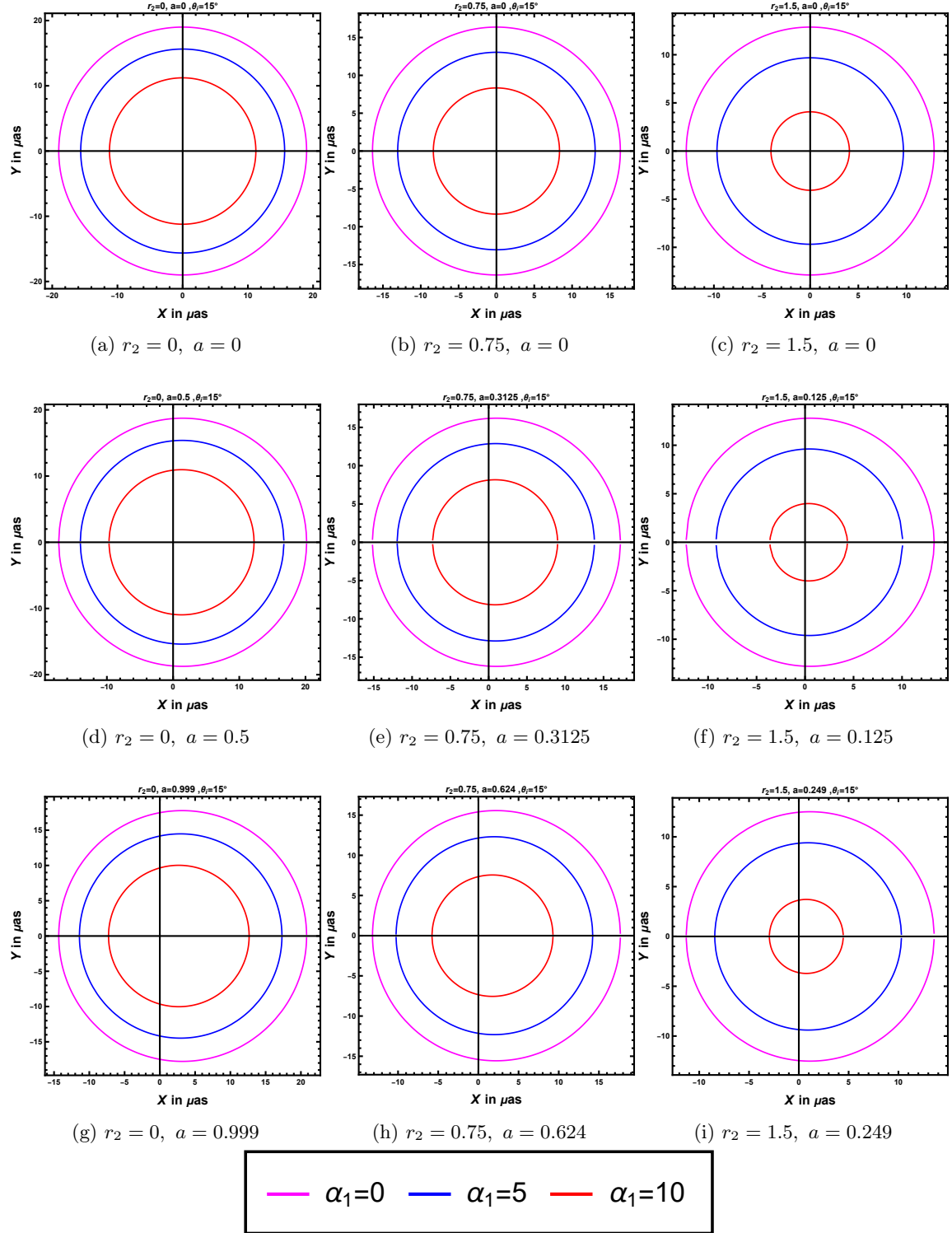


Figure 2: Variation of shadow of Kerr Sen black hole in presence of plasma profile 1 at inclination angle  $\theta_i = 15^\circ$ .



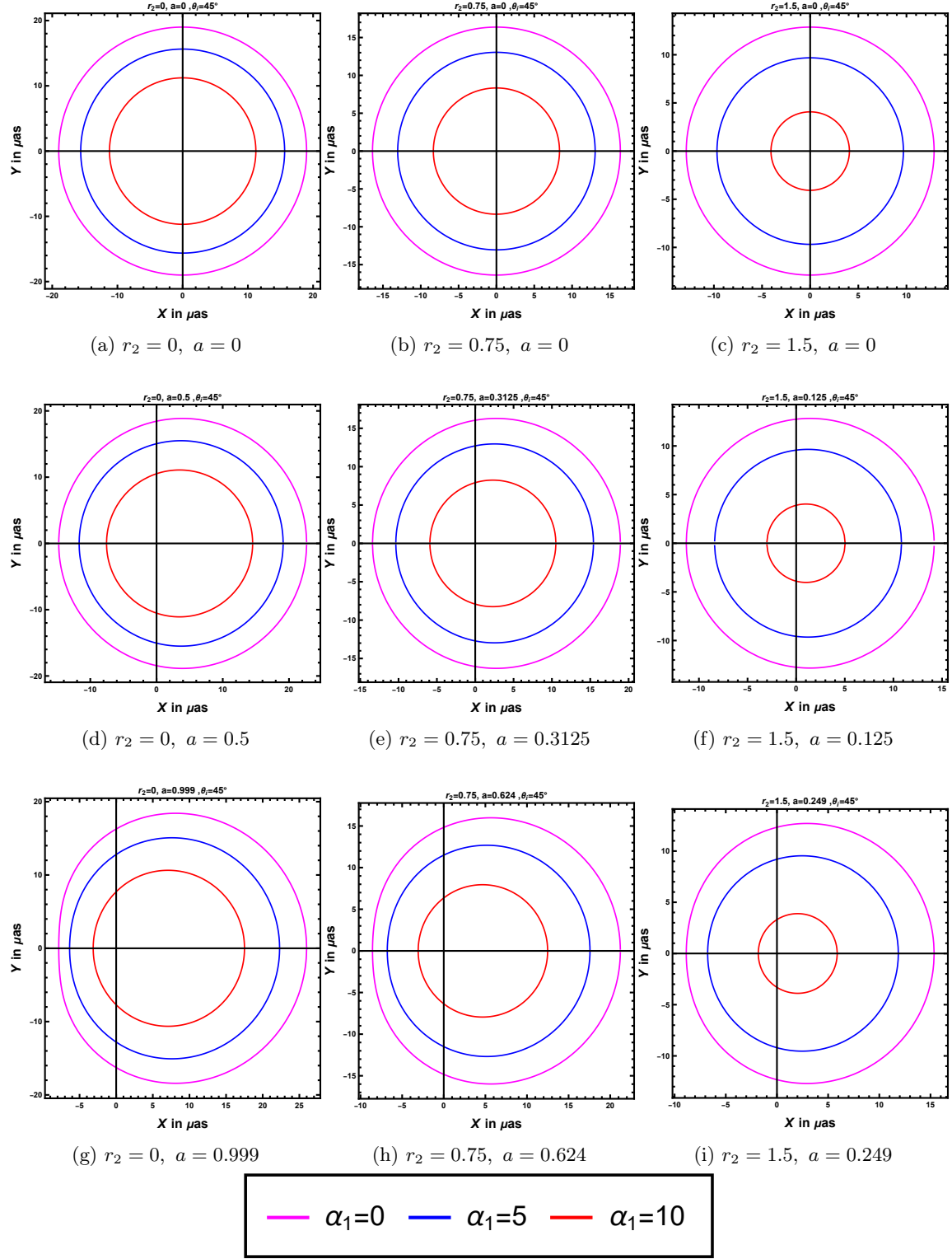


Figure 3: Variation of shadow of Kerr Sen black hole in presence of plasma profile 1 at inclination angle  $\theta_i = 45^\circ$ .

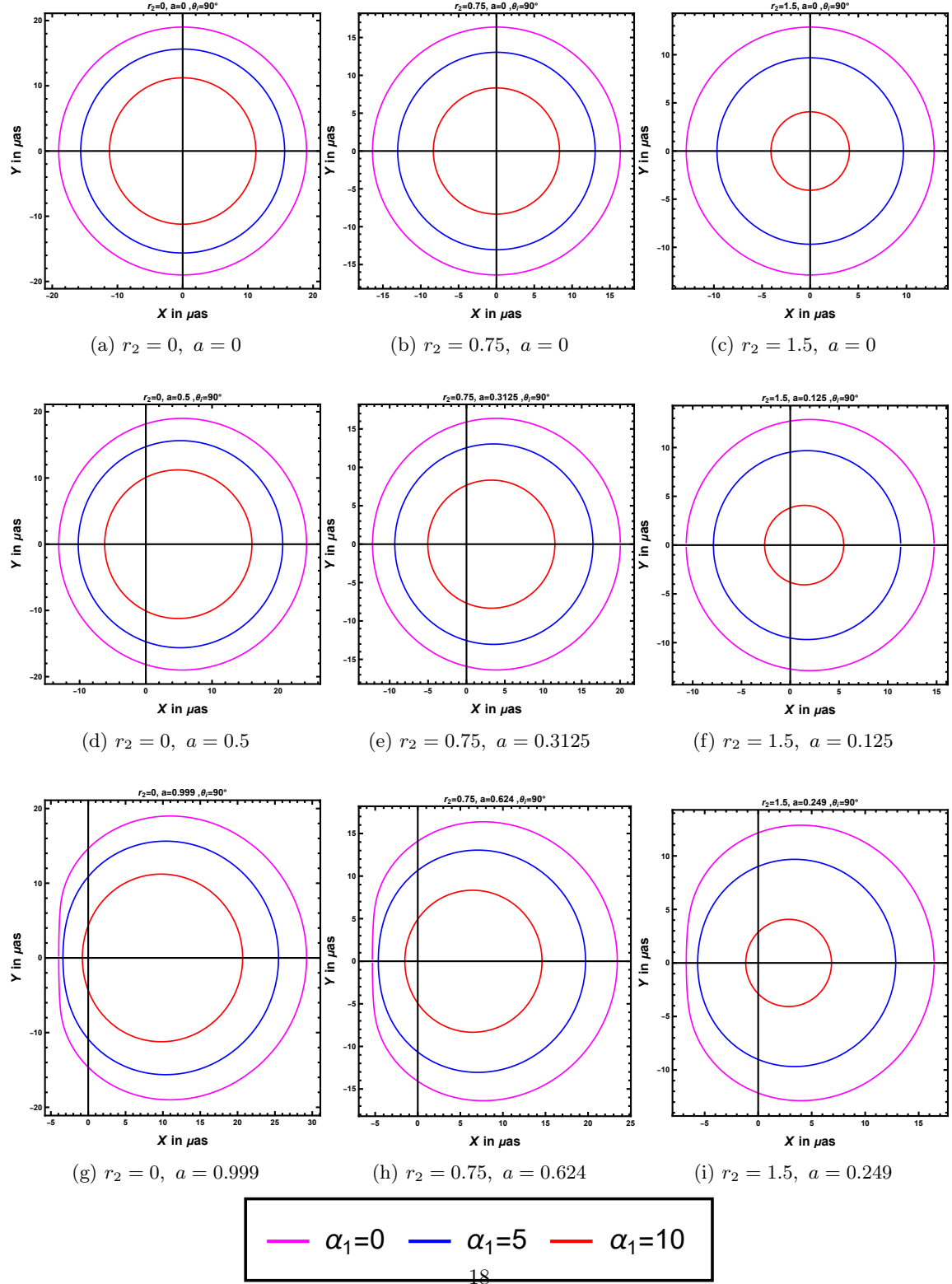


Figure 4: Variation of shadow of Kerr Sen black hole in presence of plasma profile 1 at inclination angle  $\theta_i = 90^\circ$ .

- From analysis of the Figures 3a to 3i we observe an increase in the plasma parameter  $\alpha_1$  decreases the shadow size. This effect was also observed in Figure 2.
- In addition to the contracting effect of the plasma parameter  $\alpha_1$  on the shadow size, we also observe in all the sub Figures 3a to 3i that, for sufficiently high value of  $\alpha_1$  (observe red curve in each sub figure) the shadow becomes circular irrespective of the choice of  $r_2$  and  $a$ .
- We observe that with increase in the spin  $a$  of the black hole, the shape of the shadow increasingly deviates from circular shape in addition to the shift in geometric center of the shadow. However, the effect deviation from circularity decreases with increase in  $\alpha_1$  and nearly negligible for sufficiently high values of  $\alpha_1$ .

Figure 4 shows the shadow plots for an observer in the equatorial plane.

- The contraction of shadow size due to the dilaton charge  $r_2$  and the plasma parameter  $\alpha_1$  as was observed in Figures 2 and 3 is also observed in Figure 4.
- The deviation from circularity of the shadow and the shift in the geometric center with increase in the spin  $a$  of the black hole can be observed as we go vertically downwards along each column in Figure 4. However, comparing the deviation in circularity of the shadow observed in Figures 2 to 4, we note that the shadow becomes increasingly non-circular when  $a$  and  $\theta_i$  are simultaneously increased.
- Similar to Figure 3 we note that for sufficiently high value of plasma parameter  $\alpha_1$ , the shadow becomes nearly circular irrespective of the value of  $r_2$ ,  $a$  and  $\theta_i$ .

## 4.2 Variation of shadow in case of profile 2

In this section we consider profile 2 given in Equation (74) which was discussed in [37]. The density associated with  $\omega_P^2$  in profile 2 qualitatively represents black hole accretion tori in the asymptotic limit [91–93]. In profile 2  $g(\theta) \geq 0$  which is consistent with the requirement  $\omega_P^2 \geq 0$ . The maximum value of the plasma parameter  $\alpha_2$  is determined from the Equation (72). For profile 2 we denote  $F(r, \theta)$  by  $F_2(r, \theta)$ . We plot variation of  $F_2(r, \theta)$  with  $r$  for  $r_2 = 0, 0.75$  and  $1.5$ . As  $\alpha_2$  can not exceed the minimum of  $F_2(r, \theta)$  from condition (71) thus the Figures 5a to 5c can be used to infer the bound on  $\alpha_2$ . We make the following observations from Figure 5:

- Similar to the case of profile 1 we find that for a given  $r_2$  and each case of  $a$  and  $\theta$  in Figures 5a to 5c there exists a minimum.
- The minimum of  $F_2(r, \theta)$  decreases with increase in  $\theta$  (refer Figures 5a to 5c).
- For a given  $r_2$  and  $a$  we observe that,  $F_2(r, \theta)$  (refer Figures 5a to 5c) is more sensitive to  $\theta$  compared to  $F_1(r, \theta)$  (refer Figures 1a to 1c).
- $F_2(r, \theta)$  is sensitive to  $a$  as we go near the black hole when  $\theta$  is small.
- The sensitivity of  $F_2(r, \theta)$  with respect to  $a$  decreases with increase in  $r_2$  (refer Figures 5a to 5c).

- The minimum value of  $F_2(r, \pi/2)$  gives an estimate of the maximum value of plasma parameter, that is,  $\alpha_{2max}$ .

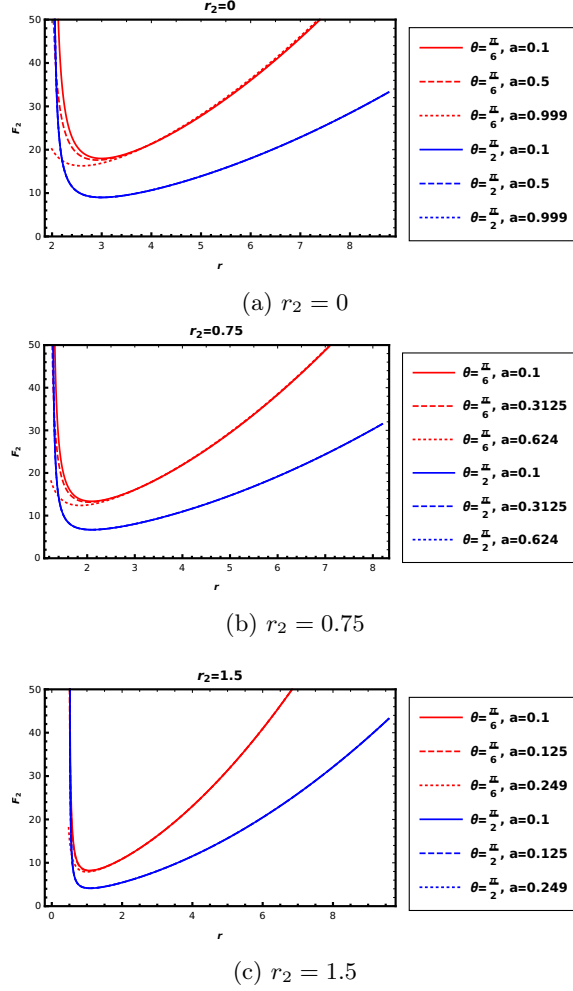


Figure 5: Variation of  $F_2(r, \theta)$  with  $r$  (in units of  $M$ ) at  $a = 0.1, 0.5(1 - \frac{r_2}{2})$  and  $0.999 - \frac{r_2}{2}$  for  $\theta = \frac{\pi}{6}$  (Red) and  $\frac{\pi}{2}$  (Blue) for different  $r_2$

- From Figures 5a to 5c we find for  $r_2 = 0, 0.75$  and  $1.5$  the corresponding  $\alpha_{2max} \approx 9, 7$  and  $4.12$ , respectively.

Furthermore, the photon region for profile 2 can be determined from Equation (41). Using  $g(\theta)$  from Equation (74) in Equation (41) we obtain

$$\frac{\mathcal{Q}(r_p)a^2 \sin^2 \theta - (-a\eta(r_p) + a^2 \sin^2 \theta)^2}{a^2 \sin^2 \theta} \geq \alpha_2(1 + 2 \sin^2 \theta) \quad (78)$$

In the above equation  $\mathcal{Q}(r_p)$  and  $\eta(r_p)$  are given by Equations (39) and (40) with  $f(r) = 0$ . The region in which the inequality (78) is satisfied is the photon region for profile 2.

We now proceed to discuss the variation of shadow of Kerr Sen black hole considering plasma profile 2 given by Equation (74). Figures 6 to 8 show the variation of shadow with  $r_2$ ,  $a$  and  $\alpha_2$  for  $\theta_i = 15^\circ, 45^\circ$  and  $90^\circ$ , respectively. The arrangement of sub-figures in Figures 6 to 8 is same as in Figures 2 to 4 (which is described in section 4.1). In each case, we can study the variation of shadow with dilaton  $r_2$  by going from left to right along each row. By going vertically downwards along each column one can study effect of  $a$  on the shadow. By comparing shadow plots for  $\alpha_2 = 0$  (Magenta curve),  $\alpha_2 = 2.06$  (Blue curve) and  $\alpha_2 = 4.12$  (Red curve) in each subfigure we can study the effect of  $\alpha_2$  on the shadow for given  $r_2$ ,  $a$  and  $\theta_i$ .

We first discuss the variation of shadow as shown in Figure 6:

- The effect of dilaton charge  $r_2$  on the shadow can be observed from Figures 6a to 6c. The increase in  $r_2$  decreases the shadow size as discussed in section 4.1. The increase in contraction due to increase of  $r_2$  is observed irrespective of the choice of  $a$  and  $\alpha_2$ . This was also observed in Figure 2, however, the contraction of shadow due to  $r_2$  in case plasma profile 2 (Figure 6) is weaker than what was observed in case of profile 1 (Figure 2) at  $\theta_i = 15^\circ$ .
- Figure 6a shows the variation of shadow purely due to plasma parameter  $\alpha_2$ . We observe that, with increase in  $\alpha_2$  there is decrease in shadow size as was observed in case of profile 1 (Figure 2a). Furthermore, the decrease in shadow size with increase in  $\alpha_2$  is observed irrespective of our choice of  $r_2$  and  $a$  (Figures 6a to 6i).
- By moving vertically downwards along each column in Figure 6 we observe that, as we increase the spin  $a$  for a given  $(r_2, \alpha_2, \theta_i)$  the geometric center of shadow shifts away from the geometric centre in case  $a = 0$ .

We next discuss the variation of shadow as shown in Figure 7 for  $\theta_i = 45^\circ$ . We observe the following:

- The previously observed effect of decrease in shadow size (refer Figures 6a to 6i) with an increase in  $r_2$  and also with  $\alpha_2$  can be observed in (refer Figures 7a to 7i).
- Moving vertically downwards along each column in Figure 7 we observe that, as we increase the spin  $a$  for a given  $(r_2, \alpha_2, \theta_i)$  the geometric centre of shadow shifts away from the geometric centre in case of  $a = 0$  and also there is deviation in circularity which increase with increase in  $a$ . But deviation in circularity in the shadow was not observed in Figures 6g to 6i where  $a$  was also increased. Thus, increase in both  $\theta_i$  and  $a$  leads to the distortion in the shape of the shadow.
- With increase in  $\alpha_2$  the deviation in circularity due to the spin  $a$  and  $\theta_i$  decreases, but the shift in the geometric center remains (refer Figures 7g to 7i). Thus, presence of plasma makes the shadow more circular irrespective of large  $a$  and  $\theta_i$ .

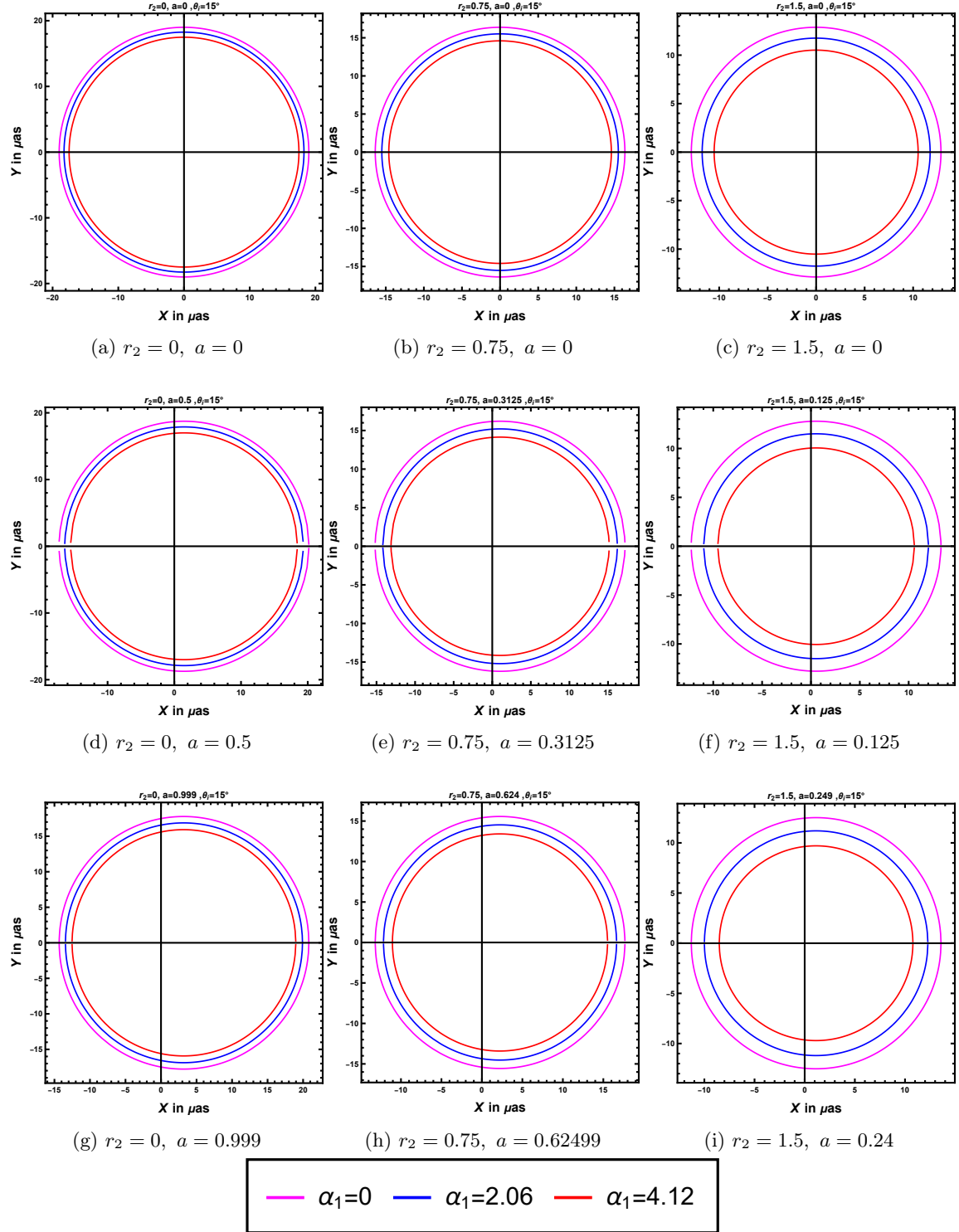


Figure 6: Variation of shadow of Kerr Sen black hole in presence of plasma profile 2 at inclination angle  $\theta_i = 15^\circ$ .

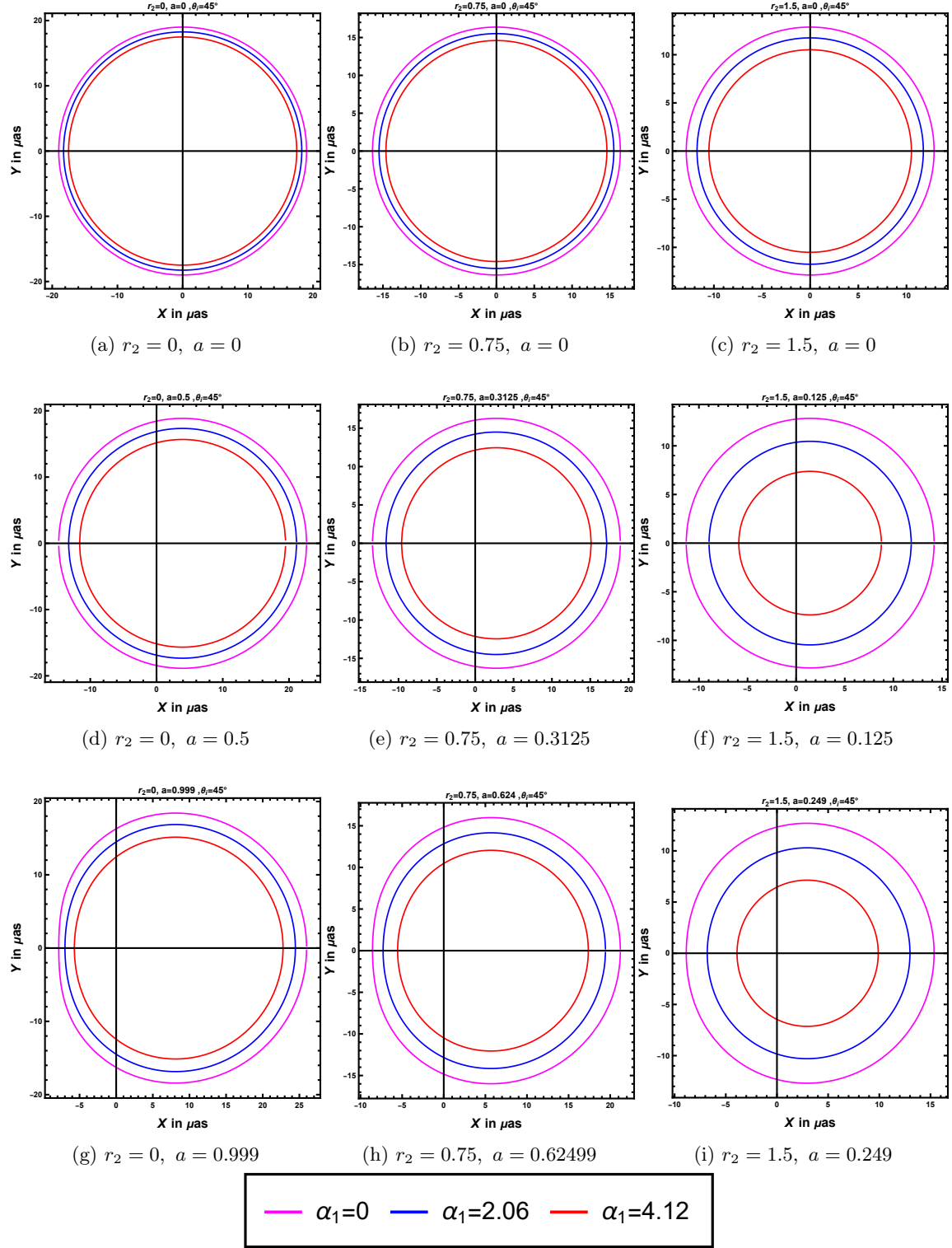


Figure 7: Variation of shadow of Kerr Sen black hole in presence of plasma profile 2 at inclination angle  $\theta_i = 45^\circ$ .

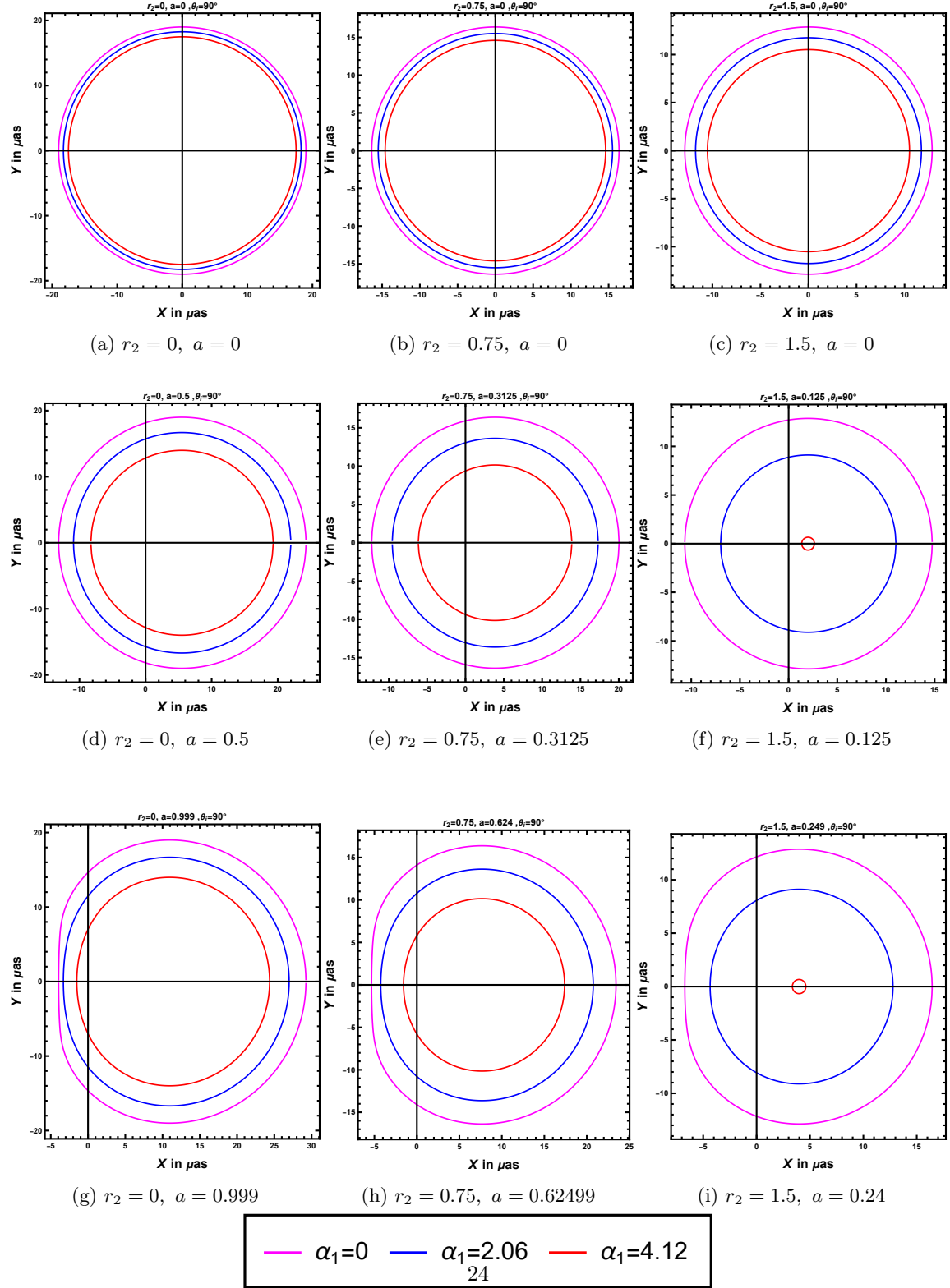


Figure 8: Variation of shadow of Kerr Sen black hole in presence of plasma profile 2 at inclination angle  $\theta_i = 90^\circ$ .



The variation of shadow as observed by an equatorial observer is shown in Figure 8. We observe the following from Figure 8:

- The generic effect of decrease in shadow size with an increase in  $r_2$  and also with  $\alpha_2$  can be observed in Figure 8.
- From comparison of Figures 8c, 8f and 8i with Figures 7c, 7f and 7i we observe that, for higher  $r_2$  the effect of contraction of shadow size due to increase in  $\alpha_2$  is more intense, for Figure 8 (i.e, at higher inclination angle).
- The combined effect of high  $\theta_i$  and  $a$  which causes increase in the deviation in circularity of shadow can be seen as we go vertically downwards along each column in Figure 8.
- As was observed in Figure 7 with increase in  $\alpha_2$  the deviation in circularity due to the spin  $a$  decreases, but the shift in the geometric centre persists (refer Figures 8g to 8i).

### 4.3 Variation of shadow outline in case of homogeneous plasma

For completeness, we now consider the case of homogeneous plasma (Equation (75)) in which the plasma density is constant. Figure 9, Figure 10 and Figure 11 plots the variation of shadow outline with  $\alpha_3$  for angle of observation  $\theta_i = 15^\circ, 45^\circ$  and  $90^\circ$  respectively. For a homogeneous plasma, Equation (72) becomes

$$\alpha_{3max} = \left(1 - \frac{2r}{\rho}\right)^{-1} \Big|_{min} \quad (79)$$

The RHS of the above equation is non negative for  $\rho > 2r$  (which is true outside the horizon). Furthermore, as  $\rho$  increases, the RHS decreases asymptotically approaching 1. Thus, for light rays to propagate to an observer at any finite distance outside the horizon in a homogeneous plasma,  $\alpha_{3max} \approx 1$ . In homogeneous plasma both unstable and stable photon orbits may exist which has been studied in [55, 94]. The unstable photon orbits are one of the main reasons behind shadow formation as light rays when perturbed in these orbits fall into the black hole. Light rays in stable photon orbits on the other hand, may continue to stay on the orbit after being perturbed and thus do not contribute in the formation of shadow.

The arrangement style of subfigures in Figures 9 to 11 is same as that in Figures 2 to 4 and Figures 6 to 8 (refer sections 4.1 and 4.2 for details). In contrary to previous profiles of non homogeneous plasma, we observe that in case of homogeneous plasma the shadow size expands with increase in  $\alpha_3$ .

From Figures 9 to 11 we can observe the following interesting features:

- From all subfigures in Figure 9, Figures 10 and 11, it is clear that with increase in  $\alpha_3$  the size of the shadow increases which is opposite to the case of profile 1 (refer section 4.1) and profile 2 (refer section 4.2).
- Unlike profile 1 and profile 2, we observe from Figures 10 and 11 that, even when we increase  $\alpha_3$  the shadow continues to be non-circular when  $a$  and  $\theta_i$  are large.

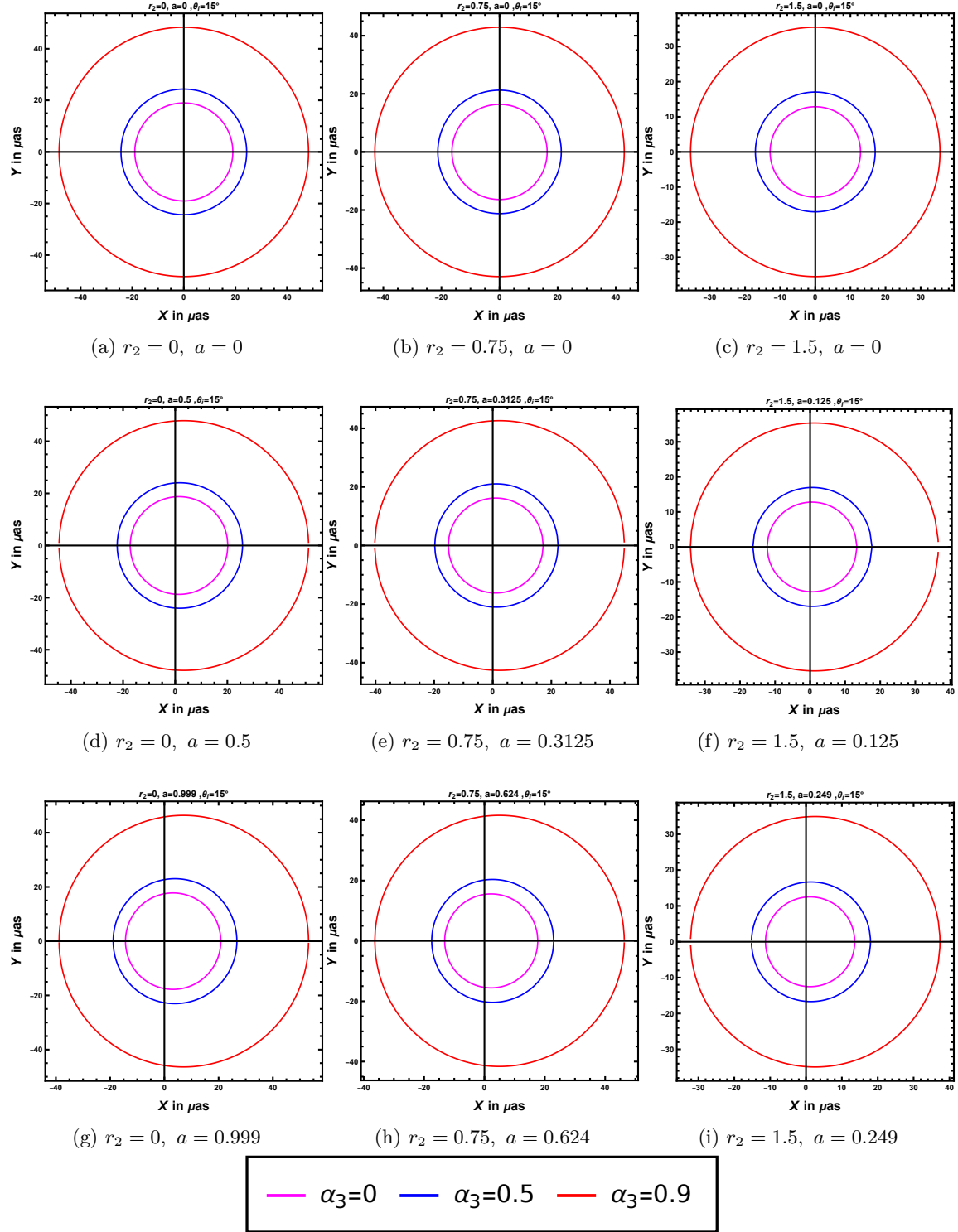


Figure 9: Variation of shadow of Kerr Sen black hole in presence of homogeneous plasma at  $\theta_i = 15^\circ$

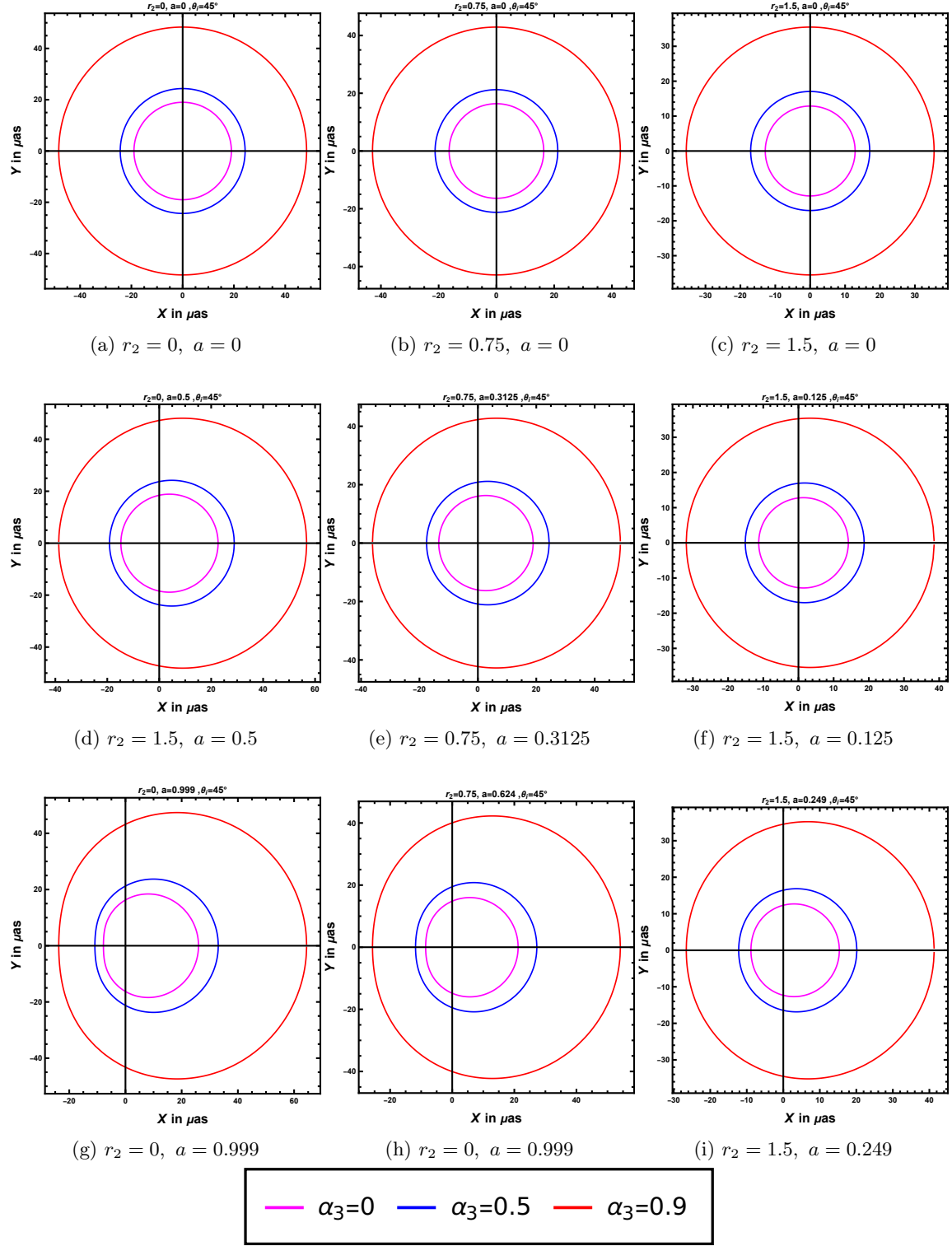


Figure 10: Variation of shadow of Kerr Sen <sup>27</sup>black hole in presence of homogeneous plasma at  $\theta_i = 45^\circ$

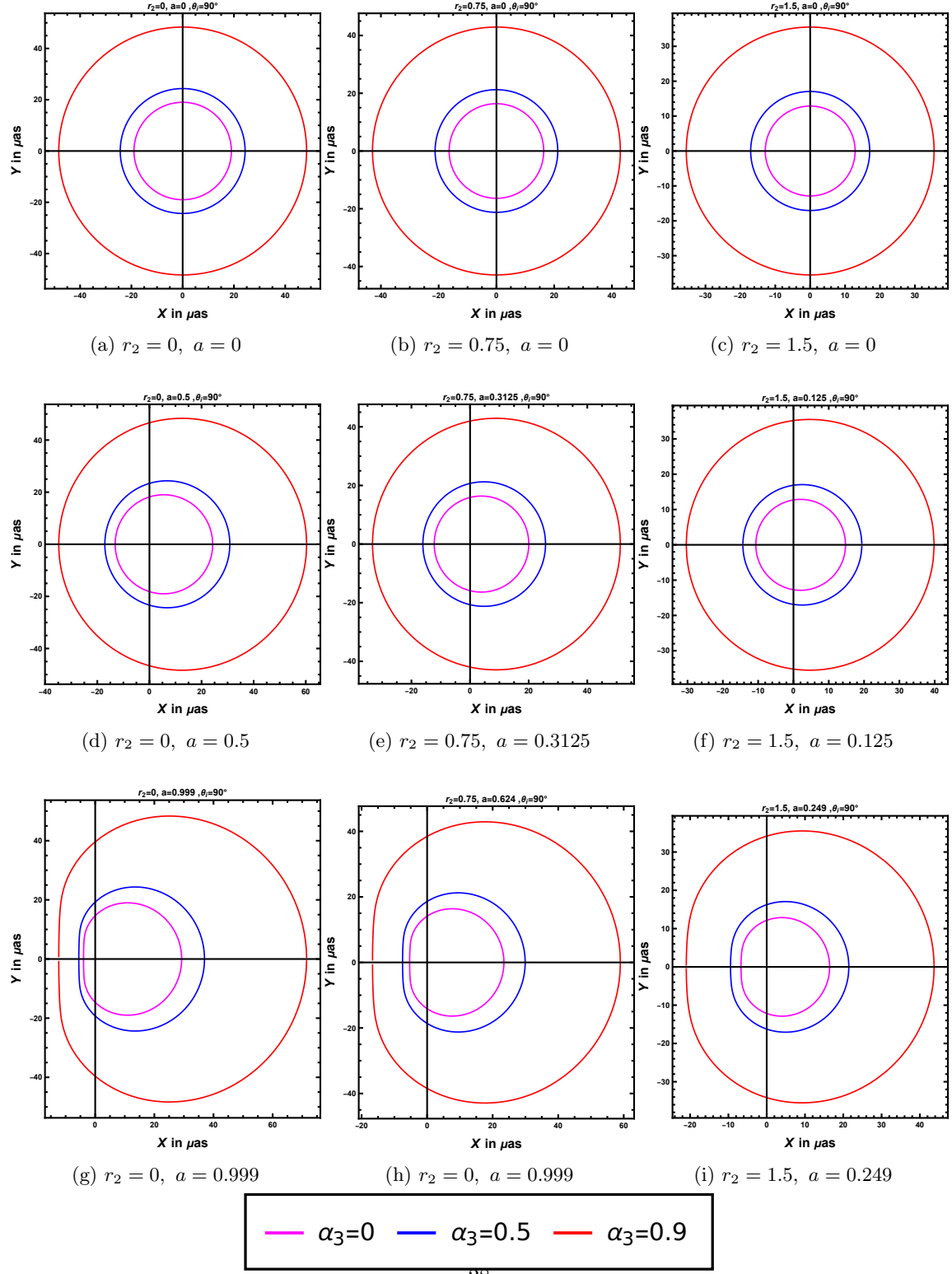


Figure 11: Variation of shadow of Kerr Sen black hole in presence of homogeneous plasma at  $\theta_i = 90^\circ$

- The decreasing of shadow size due to increase in  $r_2$  irrespective of presence or absence of plasma can be observed in Figures 9a to 9c, Figures 10a to 10c and Figures 11a to 11c. Thus, effect of  $r_2$  on the shadow is generic irrespective of the three plasma environments considered in here.

## 5 EHT observations for shadows of M87\* and Sgr A\*

In this section we first describe the observations related to shadows of M87\* and Sgr A\* as reported by the EHT collaboration. We also discuss briefly about the mass  $M$ , distance  $D$  and angle of inclination  $\theta_i$  measurements of M87\* and Sgr A\* as reported from previous observations.

For M87\*, the EHT collaboration reported the image and estimated the vertical angular diameter of the bright ring  $\Delta\Theta = (42 \pm 3)\mu\text{as}$  [4]. They also reported in [4, 5] a maximum offset of 10% between the ring diameter and the shadow (dark patch) diameter. If we take into account the maximum offset, the shadow angular diameter of M87\* is  $\Delta\Theta = (37.8 \pm 3)\mu\text{as}$ . Along with  $\Delta\Theta$ , the EHT collaboration has also reported bounds on the deviation in circularity  $\Delta C \lesssim 10\%$  [4] and the axis ratio  $\Delta A \lesssim 4/3$  [4]. Assuming M87\* as a Kerr black hole, the EHT estimated the mass of M87\* to be  $M = (6.5 \pm 0.7) \times 10^9 M_\odot$  [4, 5]. The mass of M87\* has also been previously measured,  $M = 6.2^{+1.1}_{-0.6} \times 10^9 M_\odot$  by analyzing stellar brightness and dispersion in stellar velocity [4, 95, 96]. From gas dynamics studies of M87\* the mass was estimated to be  $M = 3.5^{+0.9}_{-0.3} \times 10^9 M_\odot$  [4, 97]. The distance  $D$  and angle of inclination  $\theta_i$  for M87\*, as reported from previous measurements are  $D = (16.8 \pm 0.8)\text{Mpc}$  [98, 99] and  $\theta_i = (17 \pm 2)^\circ$  [100], respectively.

The EHT collaboration has also reported observations for image of Sgr A\*. The angular diameter estimate of the primary ring of Sgr A\* as reported by the EHT is  $\Delta\Theta = (51.8 \pm 2.3)\mu\text{as}$  [11–16] and the angular diameter of the shadow is estimated to be  $\Delta\Theta = (48.7 \pm 7)\mu\text{as}$  [14]. The mass and distance measurements of Sgr A\* have been reported by the Keck and the GRAVITY collaboration. Keeping the redshift parameter free, the Keck collaboration estimated the mass and distance of Sgr A\* to be  $M = (3.975 \pm 0.058 \pm 0.026) \times 10^6 M_\odot$  [101] and  $D = (7959 \pm 59 \pm 32)\text{pc}$  [101], respectively. When redshift parameter was set to unity the Keck collaboration reported mass  $M = (3.951 \pm 0.047) \times 10^6 M_\odot$  [101] and distance  $D = (7935 \pm 50)\text{pc}$  [101] for Sgr A\*, respectively. Another set of mass and distance measurements for Sgr A\* was reported by the GRAVITY collaboration from astrometry observations. The GRAVITY collaboration reported the mass and distance of Sgr A\* to be  $M = (4.261 \pm 0.012) \times 10^6 M_\odot$  [102, 103] and  $D = (8246.7 \pm 9.3)\text{pc}$  [102, 103], respectively. When effects of optical aberrations were taken into account, GRAVITY collaboration estimates the mass and distance of Sgr A\* to be  $M = (4.297 \pm 0.012 \pm 0.040) \times 10^6 M_\odot$  [102, 103] and  $D = (8277 \pm 9 \pm 33)\text{pc}$  [102, 103]. The angle of inclination for Sgr A\*  $\theta_i = 46^\circ$  has been estimated in [104].

In order to obtain the constraints on  $r_2$  and  $\alpha_i$  (where  $i = 1, 2, 3$  for profiles 1, 2 and 3, respectively), we follow the procedure described below:

1. We choose a plasma profile from the profiles given in Equations (73) to (75) and calculate the maximum possible value of  $\alpha_i$  using Equation (72) (refer sections 4.1 to 4.3 for details).
2. Fixing  $\alpha_i$ , we choose a value of  $0 \leq r_2 \leq 2$  and vary the spin in the allowed range  $0 \leq a \leq 1 - \frac{r_2}{2}$ . For each combination of  $\alpha_i$ ,  $r_2$  and  $a$  we calculate the theoretical vertical angular diameter  $\Delta\Theta_{th}$  for M87\* and Sgr A\* using Equation (65).

3. In order to calculate the  $\Delta\Theta_{th}$  we use previously determined mass  $M$ , distance  $D$  and angle of inclination  $\theta_i$  as discussed above. In particular, we use the central values of  $M, D$  and  $\theta_i$ .
4. We compare the observed angular diameter  $\Delta\Theta_{obs}$  with the theoretical one  $\Delta\Theta_{th}$  and calculate the  $\chi^2$  given by,

$$\chi^2 = \left( \frac{\Delta\Theta_{obs} - \Delta\Theta_{th}(\alpha_i, r_2, a_{min})}{\sigma} \right)^2 \quad (80)$$

In the above equation  $\Delta\Theta_{obs}$  and  $\sigma$  for M87\* is  $37.8\mu as$  and  $3\mu as$ , respectively. For Sgr A\*,  $\Delta\Theta_{obs} = 48.7\mu as$  and  $\sigma = 7\mu as$ .

5. The  $\chi^2$  in Equation (80) is determined by first computing  $\chi^2$  for allowed values of spin in the range  $0 \leq a \leq 1 - \frac{r_2}{2}$  for a given value of  $r_2$  and  $\alpha_i$ , and then finding the spin  $a_{min}$  corresponding to the lowest value of  $\chi^2$ . Thus,  $a_{min}$  in Equation (80) corresponds to spin for which  $\chi^2$  is minimum for a given  $\alpha_i$  and  $r_2$  [105].
6. We follow steps 2-5 for all the allowed values of  $\alpha_i$  and  $r_2$ .
7. We draw contour plots of  $\chi^2 \leq 1$  to obtain the observationally favored parameter space of  $\alpha_i$  and  $r_2$ .
8. We follow steps 2-7 for another plasma profile.

## 5.1 Constraining the dilaton charge and plasma environment from M87\* shadow

For the gas dynamics mass measurement of M87\* ( $M = 3.5 \times 10^9 M_\odot$ ),  $\Delta\Theta_{th}$  evaluated with all combinations of  $r_2$  and  $\alpha_1$  in the allowed range give  $\chi^2 > 1$  and thus, no constraints are obtained on  $r_2$  and  $\alpha_1$ . This implies that using this mass one cannot reproduce the observed angular diameter of M87\*, which possibly indicates that this mass measurement needs to be revisited. This result is also consistent with our previous finding in [46]. The constraints on  $\alpha_1$  and  $r_2$  obtained using the EHT mass measurement of M87\* (refer Figure 12b) is for the sake of comparison and completeness and should not be considered to constrain  $r_2$ . This is because the mass estimate was obtained assuming M87\* is a Kerr black hole. We now use the methodology described previously to obtain constraints on the plasma parameter  $\alpha_1$  and the dilaton charge  $r_2$  from the EHT observations of M87\*. Figures 12a and 12b show contours of  $\chi^2$  for M87\* assuming different values of  $\alpha_1$  and  $r_2$  for  $M = 6.2 \times 10^9 M_\odot$  and  $M = 6.5 \times 10^9 M_\odot$  respectively, considering plasma profile 1.

- In Figures 12a and 12b, we observe that, there is an upper bound on  $\alpha_1$  and  $r_2$  corresponding to each  $\chi^2$  contour. More importantly, in the parameter space of  $(\alpha_1, r_2)$  corresponding to the white region ( $\chi^2 > 1$ )  $\Delta\Theta_{th}$  lies beyond the  $1 - \sigma$  interval of  $\Delta\Theta_{obs}$ , and therefore values of  $r_2$  and  $\alpha_1$  corresponding to the white region are excluded outside  $1 - \sigma$ .
- In Figure 12a, for region  $\chi^2 \leq 1$  (which corresponds to  $\Delta\Theta_{th} \approx 34.8\mu as$  in the present case) we observe  $\alpha_1 \leq 2.5$  and  $r_2 \leq 0.48$ . For the region  $\chi^2 \leq 0.5$  (which corresponds to  $\Delta\Theta_{th} \approx 35.68\mu as$ ), we find  $\alpha_1 \leq 1.8$  and  $r_2 \leq 0.34$ . The the region  $\chi^2 \leq 0.1$  (which corresponds to  $\Delta\Theta_{th} \approx 36.85\mu as$ ) restricts  $\alpha_1 \leq 0.9$  and  $r_2 \leq 0.16$ . The constraints on  $\alpha_1$  and  $r_2$  obtained from the region in blue ( $\chi^2 \leq 0.1$ ) are the ones most observationally favored.

From Figure 12a we rule out  $r_2 > 0.48$  and  $\alpha_1 > 2.5$  outside  $1 - \sigma$ . We note that, the bounds on  $r_2$  obtained in our previous work [46] are consistent with the present bounds.

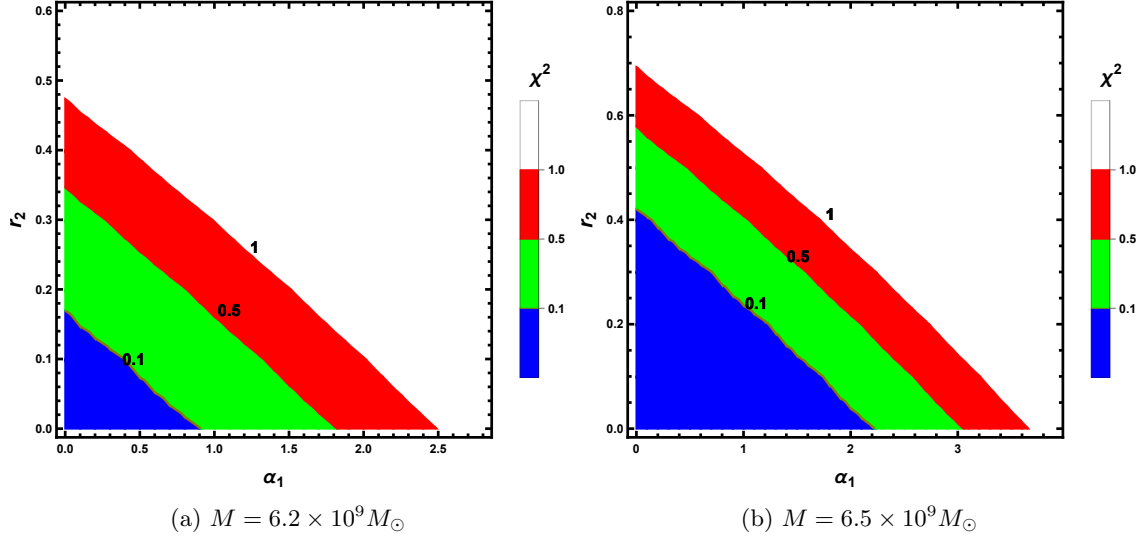


Figure 12: The figures represent contour plots of  $\chi^2$  (calculated using Equation (80) corresponding to  $a_{min}$ ) for various choices of  $\alpha_1$  and  $r_2$ , associated with plasma profile 1 for M87\*. In order to evaluate the  $\chi^2$  we use  $D = 16.8\text{Mpc}$ ,  $\theta_i = 17^\circ$  and black hole mass (a)  $M = 6.2 \times 10^9 M_\odot$  and (b)  $M = 6.5 \times 10^9 M_\odot$  (EHT estimate). In the figures, the red color region in the  $\alpha_1 - r_2$  plane corresponds to  $0.5 \leq \chi^2 \leq 1$ , the region with  $0.1 \leq \chi^2 \leq 0.5$  is colored green and the blue region represents  $0 \leq \chi^2 \leq 0.1$ .

- For stellar dynamics mass measurement  $\alpha_1 = 0.1, r_2 = 0$  and  $a = 0.2$  gives the lowest  $\chi^2$ . Also, for  $\chi^2 \leq 1$  the allowed spin range is  $0.1 \leq a \leq 0.3$ . For completeness, when mass estimate by the EHT collaboration was considered,  $\alpha_1 = 1.3, r_2 = 0$  and  $a = 0.4$  gave lowest  $\chi^2$  and the allowed spin range for  $\chi^2 \leq 1$  is  $0.1 \leq a \leq 0.9$ .
- For each  $\chi^2$  contour in Figures 12a and 12b we observe that, as  $\alpha_1$  is increased in the allowed range, the upper bound on  $r_2$  corresponding to the  $\alpha_1$ , keeps decreasing and vice-versa. This is an artifact of the decreasing effect produced due to  $\alpha_1$  and  $r_2$  on the shadow size (refer Figures 2 to 4).
- We further observe that there is only one contour for each  $\chi^2$  in contrast with Figures 14a to 14c for homogeneous plasma (for example, contours of  $\chi^2 = 0.1$  appears twice). This is because in the case of plasma profile 1 both  $\alpha_1$  and  $r_2$  have a contracting effect on the shadow size, whereas homogeneous plasma has expanding effect on the shadow. Therefore the upper  $1 - \sigma$  value of  $\Delta\Theta_{obs}$  is not obtained for any  $(\alpha_1, r_2)$  using mass measurements in Figures 12a and 12b.

Next we discuss the constraints on the dilaton charge  $r_2$  and  $\alpha_2$  for plasma profile 2 using the EHT observations of M87\*. In Figures 13a and 13b, the  $\chi^2$ - contour plots for M87\* considering

plasma profile 2 are given. For reasons already discussed in case of profile 1 previously, we will consider constraints obtained from Figure 13a only. In case of profile 2 also we obtain  $\chi^2 > 1$  for all choices of  $\alpha_2$  and  $r_2$  when gas dynamics mass measurement of M87\* is considered, and thus we get no constraints. Hence, the inability to reproduce the observed shadow angular diameter of M87\* with this mass ( $M = 3.5 \times 10^9 M_\odot$ ) which was highlighted in our previous work [46] is consistent with plasma profile 2 as well. Furthermore, the mass of M87\* estimated from gas dynamics measurement is clearly not in agreement with the EHT constraint  $M = 6.5 \times 10^9 M_\odot$ . The constraints on the dilaton parameter and the plasma parameter are very similar to that of profile 1.

In Figure 13a, from the region  $\chi^2 \leq 1$  (which in case of profile 2 will represent the lower  $1 - \sigma$  value of  $\Delta\Theta_{obs}$  for M87\*) we find  $\alpha_2 \leq 3.8$  and  $r_2 \leq 0.48$ . However, the upper bound of  $\alpha_2$  is more than that of  $\alpha_1$  in Figure 12a. For the region  $\chi^2 \leq 0.5$  in Figure 13a we obtain the upper bounds on  $\alpha_2 \leq 2.8$  and  $r_2 \leq 0.34$ . From the region  $\chi^2 \leq 0.1$  (which is most observationally favored) we obtain  $\alpha_2 \leq 1.4$  and  $r_2 \leq 0.16$ . We again observe that the upper bounds on  $\alpha_2$  are more than the upper bounds of  $\alpha_1$ . This is because, profile 1 has a stronger contraction effect on the shadow size compared to profile 2 in case of M87\* (see Sections 4.1 and 4.2). This result is sensitive to the mass and distance of the black hole and hence may not be generic (Equations (63) to (65)). For profile 2, when mass measurement from stellar dynamics is considered  $\alpha_2 = 0.2, r_2 = 0$  and  $a = 0.1$  gives the lowest  $\chi^2$  and the allowed range of spin for  $\chi^2 \leq 1$  is  $0 \leq a \leq 0.3$ . When mass estimated by the EHT collaboration is used  $\alpha_2 = 2.2, r_2 = 0$  and  $a = 0.2$  gives the lowest  $\chi^2$  and the allowed range of spin within  $\chi^2 \leq 1$  in this case,  $0 \leq a \leq 0.9$ .

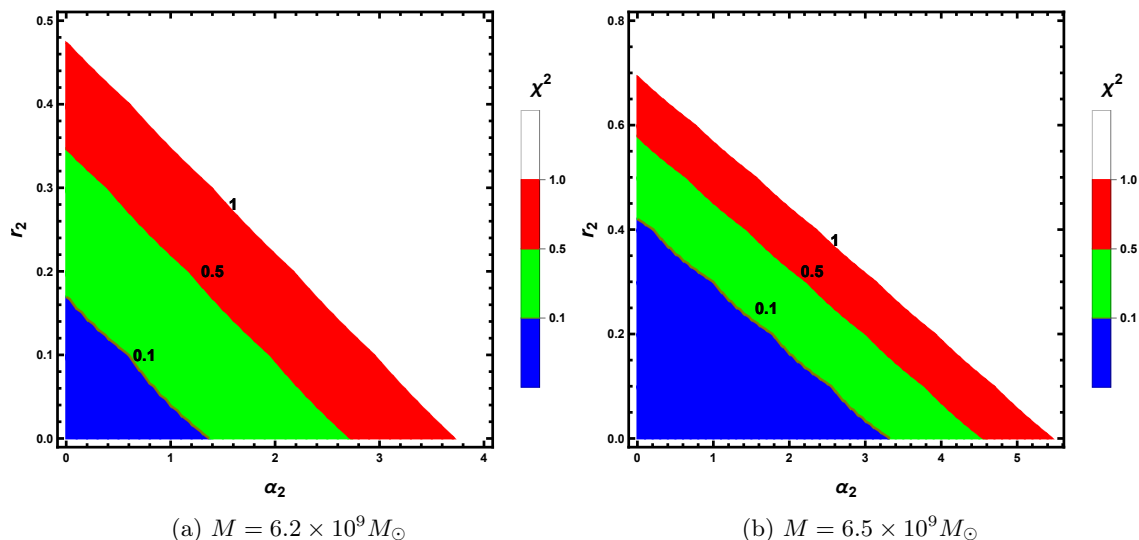


Figure 13: The figures represent contour plots of  $\chi^2$  (calculated using Equation (80) corresponding to  $a_{min}$ ) for various choices of  $\alpha_2$  and  $r_2$ , corresponding to plasma profile 2 for M87\*. In order to evaluate the  $\chi^2$  we use  $D = 16.8 \text{Mpc}$ ,  $\theta_i = 17^\circ$  and black hole mass (a)  $M = 6.2 \times 10^9 M_\odot$  and (b)  $M = 6.5 \times 10^9 M_\odot$ . In the figures, the red color region in  $\alpha_1 - r_2$  plane corresponds to  $0.5 \leq \chi^2 \leq 1$ , the region with  $0.1 \leq \chi^2 \leq 0.5$  is colored green and the blue region represents  $0 \leq \chi^2 \leq 0.1$ .

From our results obtained from Figures 12 and 13, we can say that the presence of plasma



affects the constraints on the dilaton charge, because of the dispersive effect of the plasma on the shadow. Secondly, in both cases (plasma profiles 1 and 2), the highest bound on  $\alpha_1$  and  $\alpha_2$  obtained from the EHT observations is far less than the theoretical upper bounds on  $\alpha_1$  and  $\alpha_2$  (Equations (70) and (72) and Figures 1 and 5). This means that high plasma densities are not favored by the EHT observations of M87\* when profiles 1 and 2 are considered. Also, for the highest value of plasma parameters  $\alpha_1$  and  $\alpha_2$ , we get  $r_2 \approx 0$  (for all  $\chi^2$  contours). Thus, higher density plasma environments described by profile 1 and 2 favor Kerr black hole compared to Kerr Sen black hole scenario. Furthermore, the persistence of M87\* shadow [106] indicates that the effect of the metric on the shadow diameter is predominant compared to the accretion environment. Our analysis indicates that, the spin estimate for M87\* based on stellar dynamics mass measurements is  $0 \lesssim a \leq 0.3$  and from the EHT mass estimate is  $0 \leq a \leq 0.9$ . The constraints on spin are more or less same in case of profile 1 and profile 2. The spin of M87\* has been estimated previously based on jet power in [107] to be  $|a| \geq 0.4$  (in prograde case) and  $|a| \geq 0.5$  (in retrograde case) and Tamburini et al. [100] reported the spin to be  $a = 0.9 \pm 0.05$  with approximately 95% confidence level. These previous estimates are higher than spin constraints obtained by us using stellar dynamics mass estimate of M87\*. It must be noted that, constraining the spin of a black hole from its shadow is not easy as the angular diameter of the shadow is not very sensitive to the spin particularly when the inclination angle is low (which is  $17^\circ$  for M87\*) (refer Sections 4.1 and 4.2). Also in the Kerr black hole case the maximum variation of angular diameter of the shadow is 4% for the allowed spin range [107–109]. Our results based on profile 1 and profile 2 indicate that the EHT data for M87\* favors the Kerr black hole scenario although Kerr Sen black hole with dilaton charge  $r_2 \leq 0.48$  is allowed within  $1 - \sigma$ .

We now consider the homogeneous plasma case, where we have reported contour plots considering gas dynamics, stellar dynamics and the EHT mass measurement in Figures 14a to 14c respectively. We highlight some distinct features of the contour plots in case of homogeneous plasma.

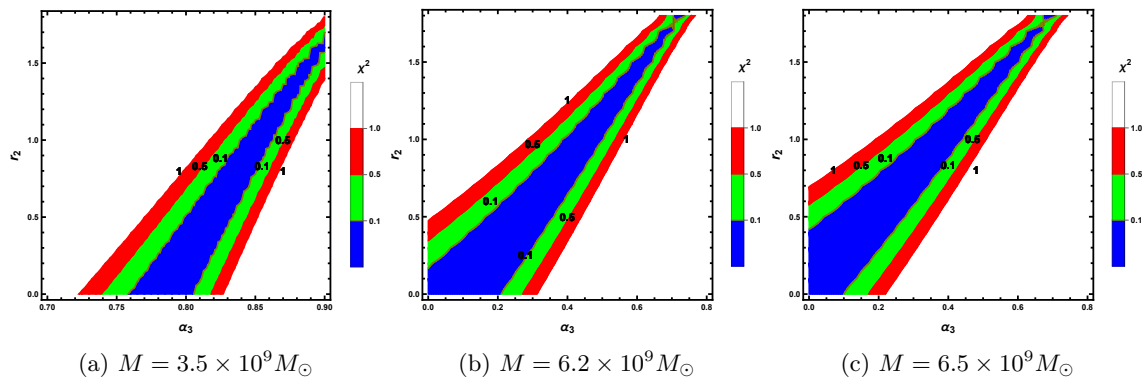


Figure 14: The figures represent contour plots of  $\chi^2$  (calculated using Equation (80) corresponding to  $a_{min}$ ) for (a)  $M = 3.5 \times 10^9 M_\odot$ , (b)  $M = 6.2 \times 10^9 M_\odot$  and (c)  $M = 6.5 \times 10^9 M_\odot$  for M87\* surrounded by homogeneous plasma. In the figures, the red color region of  $\alpha_1 - r_2$  plane corresponds to  $0.5 \leq \chi^2 \leq 1$ , the region with  $0.1 \leq \chi^2 \leq 0.5$  is colored green and the blue region represents  $0 \leq \chi^2 \leq 0.1$ . For the figures the distance  $D = 16.8 \text{ Mpc}$  and angle of inclination  $\theta_i = 17^\circ$ .

- We observe that each contour plot in Figures 14a to 14c has two contours corresponding to

each  $\chi^2 = 0.1, 0.5$  and  $1$ . This happens because the homogeneous plasma parameter  $\alpha_3$  has an expanding effect on the shadow size which can dominate over contracting effect produced due to  $r_2$  (refer Figures 9 to 11). This allows one to reproduce the  $\chi^2$  corresponding to the upper  $1 - \sigma$  and the lower  $1 - \sigma$  bounds related to  $\Delta\Theta_{obs}$ .

- Secondly, here we observe from Figure 14a, unlike the case of profile 1 and profile 2, when homogeneous plasma is considered, even considering the gas dynamics mass measurement for M87\* one can produce the the central as well as  $1 - \sigma$  values of  $\Delta\Theta_{obs} = (37.8 \pm 3)\mu as$ . This is possible because, although a smaller mass decreases the shadow (one of the causes of smaller shadow size [46]), the expansive effect of  $\alpha_3$  allows one to reproduce  $\Delta\Theta_{obs}$ .
- When  $\alpha_3 \leq 0.72$ , we fail to reproduce  $\Delta\Theta_{obs}$  within  $1 - \sigma$ . For  $\alpha_3 > 0.83$  a non-zero  $r_2$  is required to explain the observed shadow.
- We now consider  $M = 6.2 \times 10^9 M_\odot$  to obtain  $\Delta\Theta_{th}$ . Since, mass has an increasing effect on the shadow we require smaller  $\alpha_3$  to reproduce  $\Delta\Theta_{obs}$  (compare Figures 14a and 14b). For a given  $\alpha_3$ , this mass allows us to encompass larger  $r_2$  (Figures 14a and 14b), since  $M$  and  $\alpha_3$  increase the shadow, and  $r_2$  decreases the shadow. Same observation holds good for Figure 14c with  $M = 6.5 \times 10^9 M_\odot$ .

## 5.2 Constraining the dilaton charge and plasma environment from Sgr A\* shadow

We now use the methodology to obtain constraints on the dilaton charge  $r_2$  and  $\alpha_1$  (profile 1) for Sgr A\* using the EHT observations of its shadow. The EHT collaboration reported the angular diameter of the shadow to be  $\Delta\Theta_{obs} = (48.7 \pm 7)\mu as$ . Figures 15a to 15d show the contours of  $\chi^2$  for Sgr A\* considering plasma profile 1 for previously reported mass and distance measurements. Figures 15a and 15b are plotted using Keck team measurements [101]  $M = 3.951 \times 10^6 M_\odot$ ,  $D = 7935 pc$  and  $M = 3.975 \times 10^6 M_\odot$ ,  $D = 7959 pc$ , respectively. Figures 15c and 15d are plotted using GRAVITY collaboration measurements [102, 103]  $M = 4.261 \times 10^6 M_\odot$ ,  $D = 8246.7 pc$  and  $M = 4.297 \times 10^6 M_\odot$ ,  $D = 8277 pc$ , respectively.

- The contour plots in Figure 15 and Figure 12 are similar in nature. For each  $\chi^2$  contour, as  $\alpha_1$  increases in the allowed range, the upper bound of  $r_2$  decreases and vice-versa.
- In Figures 15a and 15b,  $\alpha_1 \leq 5.2$  and  $r_2 \lesssim 1$  is allowed within  $1 - \sigma$  (which corresponds to  $\Delta\Theta_{th} \gtrsim 41.7\mu as$ ). We obtain the bounds,  $\alpha_1 \leq 4.2$  and  $r_2 \leq 0.8$ , when  $\chi^2 \leq 0.5$  (which corresponds to  $\Delta\Theta_{th} \gtrsim 43.75\mu as$ ). For the most observationally favored region  $\chi^2 \leq 0.1$  (corresponding to  $\Delta\Theta_{th} \gtrsim 46.49\mu as$ ),  $\alpha_1 \leq 2.8$  and  $r_2 \leq 0.5$ . Furthermore,  $\alpha_1 > 5.2$  and  $r_2 > 1$  are ruled outside of  $1 - \sigma$ .
- For the Keck team mass and distance measurement  $M = 3.951 \times 10^6 M_\odot$ ,  $D = 7935 pc$ ,  $\alpha_1 = 0.3$ ,  $r_2 = 0.2$  and  $a = 0.45$  gives lowest  $\chi^2$  and for the mass and distance measurement  $M = 3.975 \times 10^6 M_\odot$ ,  $D = 7959 pc$ ,  $\alpha_1 = 1.2$ ,  $r_2 = 0$  and  $a = 0.7$  gives lowest  $\chi^2$ . However, for both measurements, the allowed range of spin within  $\chi^2 \leq 1$  is  $0 \lesssim a \leq 1$ .

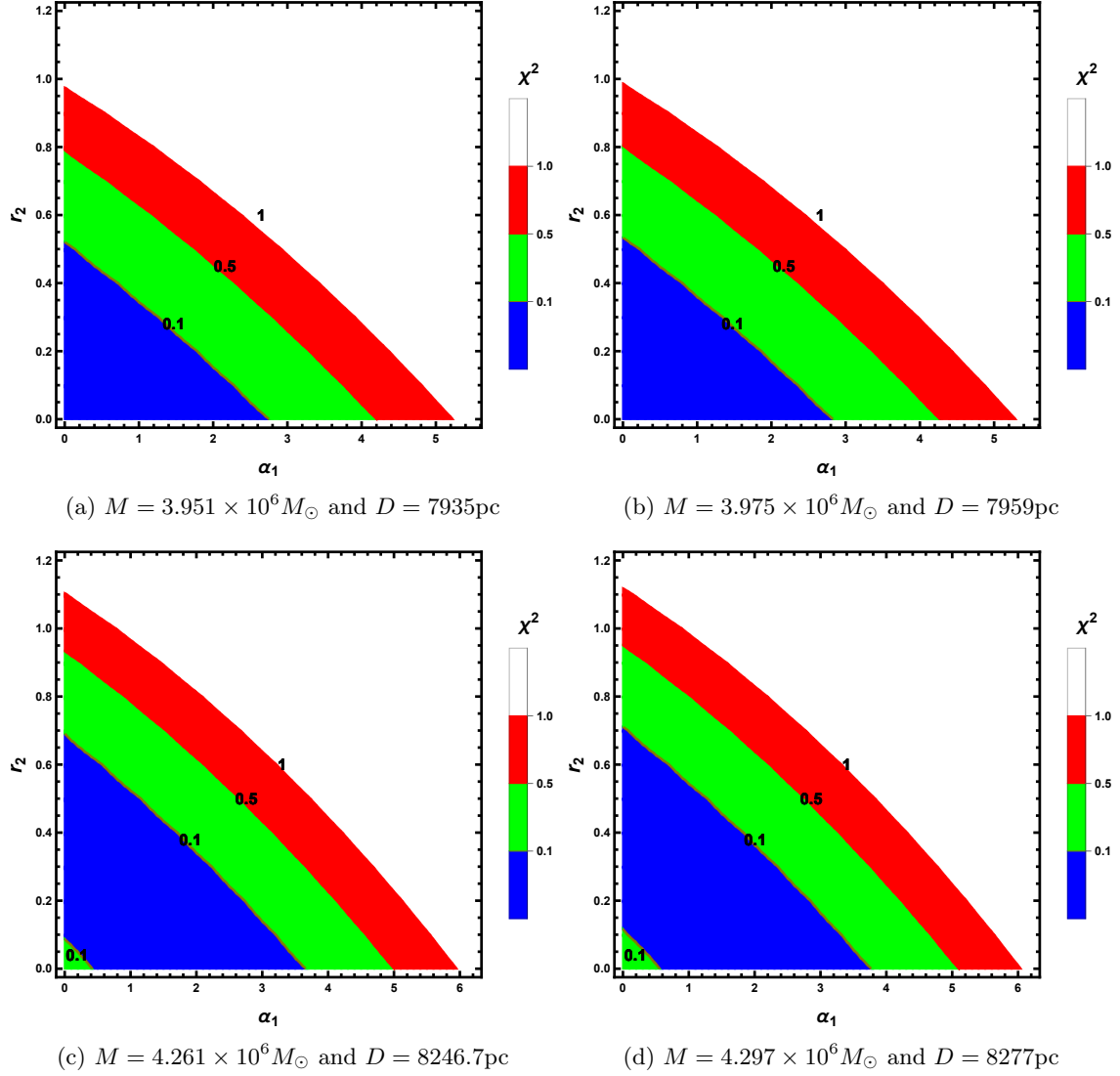


Figure 15: The figures represent contour plots of  $\chi^2$  (calculated using Equation (80) corresponding to  $a_{min}$ ) for Keck (Figures 15a and 15b) and GRAVITY collaboration (Figures 15c and 15d) mass and distance measurements for Sgr A\* surrounded by plasma profile 1. In the figures, the red color region of  $\alpha_1 - r_2$  plane corresponds to  $0.5 \leq \chi^2 \leq 1$ , the region with  $0.1 \leq \chi^2 \leq 0.5$  is colored green and the blue region represents  $0 \leq \chi^2 \leq 0.1$ . For all figures the angle of inclination  $\theta_i = 46^\circ$ .

- In Figures 15c and 15d,  $\alpha_1 \leq 6$  and  $r_2 \leq 1.1$  for the region  $\chi^2 \leq 1$ . For the region  $\chi^2 \leq 0.5$  we obtain the bounds,  $\alpha_1 \lesssim 5$  and  $r_2 \lesssim 0.9$ . For the most observationally favored region  $\chi^2 \leq 0.1$ , we obtain  $0.4 \leq \alpha_1 \leq 3.6$  and  $0.1 \leq r_2 \leq 0.7$ . This implies that for  $\Delta\Theta_{th}$  evaluated by using the mass  $M$  and distance  $D$  reported by the GRAVITY collaboration,  $r_2 = 0$  is not most

observationally favored. This is further supported by our finding that, for mass and distance measurement  $M = 4.261 \times 10^6 M_\odot$ ,  $D = 8246.7\text{pc}$ ,  $\alpha_1 = 0.9$ ,  $r_2 = 0.2$  and  $a = 0.81$  gives the lowest  $\chi^2$ . Also when mass and distance measurement  $M = 4.297 \times 10^6 M_\odot$ ,  $D = 8277\text{pc}$  is considered,  $\alpha_1 = 1.6$ ,  $r_2 = 0.2$  and  $a = 0.27$  gives the lowest  $\chi^2$ .

- Furthermore for the mass and distance measurements,  $(M = 4.261 \times 10^6 M_\odot, D = 8246.7\text{pc})$  we get  $0.1 \leq a \leq 1$  and for  $(M = 4.297 \times 10^6 M_\odot, D = 8277\text{pc})$  we get  $0 \leq a \leq 1$  as the allowed spin within  $1 - \sigma$ .

We next consider the case of profile 2. The contours for  $\chi^2$  for different mass and distance measurements of Sgr A\* are shown in Figures 16a to 16d.

- Similar to the case of profile 1, the contour plots in Figure 13 and Figure 16 are similar in nature. For a given contour, as  $\alpha_2$  increases in the allowed range the upper bound of  $r_2$  decreases and vice-versa.
- In Figures 16a and 16b,  $\alpha_2 \leq 4.4$  and  $r_2 \lesssim 1$  for the region  $\chi^2 \leq 1$ . For the region  $\chi^2 \leq 0.5$ , we obtain the bounds,  $\alpha_2 \leq 3.6$  and  $r_2 \leq 0.8$ . For the most observationally favored region  $\chi^2 \leq 0.1$ ,  $\alpha_2 \leq 2.4$  and  $r_2 \leq 0.5$ . Furthermore,  $\alpha_1 > 4.4$  and  $r_2 > 1$  are ruled outside  $1 - \sigma$ .
- For the Keck team the mass and distance estimate  $M = 3.951 \times 10^6 M_\odot$ ,  $D = 7935\text{pc}$ ,  $\alpha_2 = 0.4$ ,  $r_2 = 0.1$  and  $a = 0.76$  gives the lowest  $\chi^2$  and for the mass and distance estimate  $M = 3.975 \times 10^6 M_\odot$  and  $D = 7959\text{pc}$ ,  $\alpha_2 = 1.3$ ,  $r_2 = 0$  and  $a = 0.3$  gives the lowest  $\chi^2$ .
- In Figures 16c and 16d,  $\alpha_2 \lesssim 5.2$  and  $r_2 \leq 1.1$  for the region  $\chi^2 \leq 1$ . For region  $\chi^2 \leq 0.5$  we obtain the bounds,  $\alpha_2 \lesssim 4.4$  and  $r_2 \lesssim 0.95$ . For the most observationally favored region  $\chi^2 \leq 0.1$ , we obtain  $0.4 \leq \alpha_2 \leq 3.2$  and  $0.1 \leq r_2 \leq 0.7$ . In the case of profile 2 also we observe that the Kerr scenario is not most observationally favored although it is allowed within  $1 - \sigma$ . Furthermore,  $\alpha_1 > 5.2$  and  $r_2 > 1.1$  are ruled outside  $1 - \sigma$ .
- For the GRAVITY collaboration estimates  $M = 4.261 \times 10^6 M_\odot$ ,  $D = 8246.7\text{pc}$ ,  $\alpha_2 = 1.2$ ,  $r_2 = 0.2$  and  $a = 0.27$  gives the lowest  $\chi^2$  and for  $M = 4.297 \times 10^6 M_\odot$ ,  $D = 8277\text{pc}$ ,  $\alpha_2 = 0$ ,  $r_2 = 0.5$  and  $a = 0.075$  gives the lowest  $\chi^2$ .
- For all the Keck team and GRAVITY collaboration mass measurements the allowed range of spin within  $\chi^2 \leq 1$  is  $0 \leq a \leq 1$ .

From the constraints obtained for Sgr A\* on the plasma parameters  $\alpha_1$  and  $\alpha_2$  and the dilaton parameter  $r_2$  considering profile 1 and profile 2 we note that very high plasma densities are not favored in both cases. Interestingly, for the case of Sgr A\* we find in general, the bounds of  $\alpha_2$  (Figure 16) are less than the bounds on  $\alpha_1$  (Figure 15). This, indicates profile 2 has stronger contracting effect on the shadow than profile 1 which is contrary to what we observed in case of M87\* (refer Sections 4.1, 4.2 and 5.1). Thus, the contracting effects of profile 1 and profile 2 are sensitive to mass  $M$  and distance  $D$ .

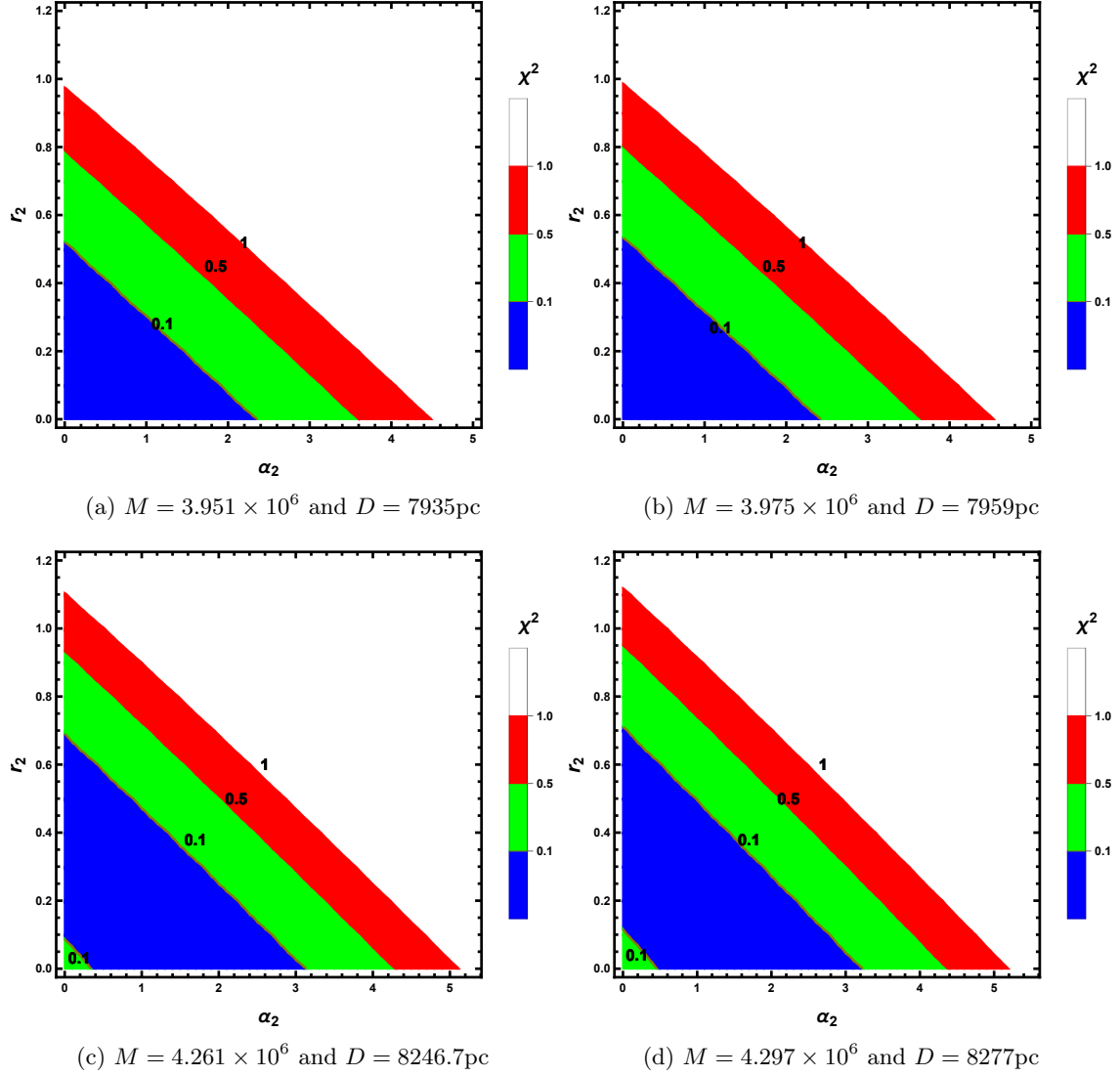


Figure 16: The figures represent contour plots of  $\chi^2$  (calculated using Equation (80) corresponding to  $a_{min}$ ) for Keck (Figures 16a and 16b) and GRAVITY collaboration (Figures 16c and 16d) mass and distance measurements for Sgr A\* surrounded by plasma profile 2. In the figures, the red color region of  $\alpha_1 - r_2$  plane corresponds to  $0.5 \leq \chi^2 \leq 1$ , the region with  $0.1 \leq \chi^2 \leq 0.5$  is colored green and the blue region represents  $0 \leq \chi^2 \leq 0.1$ . For all figures the angle of inclination  $\theta_i = 46^\circ$ .

The constraints on the plasma parameter and the dilaton charge corresponding to two sets of distance and mass measurements reported by the Keck team ( $r_2 > 1$  and  $\alpha_1 > 5.2$  ruled outside  $1 - \sigma$  for profile 1 and  $r_2 > 1$  and  $\alpha_1 > 4.4$  ruled outside  $1 - \sigma$  for profile 2) are nearly same because of small variation in these measurements. This is also the case for the constraints obtained from the

mass and distance measurements reported by the GRAVITY collaboration ( $r_2 > 1.1$  and  $\alpha_1 > 6$  for profile 1 and  $r_2 > 1.1$  and  $\alpha_1 > 5.2$  for profile 2). More importantly using mass and distance measurements by GRAVITY collaboration, we find for the plasma profiles 1 and 2 an allowed range of plasma parameters ( $\alpha_1 \lesssim 0.45$  and  $\alpha_2 \lesssim 0.4$ ) for which the most observationally favored region excludes the Kerr scenario. This is not observed when Keck team's mass and distance measurements are used. It is worth mentioning when the dilaton charge was constrained using  $\Delta\Theta_{obs} = 48.7\mu as$  by the EHT collaboration and  $M$  and  $D$  reported by the GRAVITY collaboration, a non zero dilaton  $r_2$  was favored even without plasma [46]. The allowed spin range within  $\chi^2 \leq 1$  using both mass and distance estimates by the Keck team and the GRAVITY collaboration is  $0 \lesssim a \lesssim 1$  for both plasma profiles 1 and 2. Thus, the shadow observation fails to provide strong constraints on spin of Sgr A\*. There are various spin estimates of Sgr A\* reported previously in literature. The spin of Sgr A\* was estimated to be  $a \sim 0.92$  in [110],  $a \sim 0.5$  in [111],  $a \lesssim 0.1$  in [112],  $a \sim 0.22$  in [113],  $a > 0.4$  [114],  $a \sim 0.52$  in [115] and  $a = 0.9 \pm 0.06$  in [116]. Clearly, these previous spin estimates are not consistent. Lastly, one important finding for both cases of plasma profiles 1 and 2 is that, for plasma environments with higher density, present shadow observations disfavor higher dilaton charges. This was also observed in the case of M87\* (refer Section 5.1).

We now proceed to discuss the case of homogeneous plasma. In Figures 17a to 17d we observe the following

- Because of the expansive effect of homogeneous plasma on the shadow (refer Figures 9 to 11) we can reproduce both the upper  $1 - \sigma$  and lower  $1 - \sigma$  values of  $\Delta\Theta_{th}$ . Hence, we get two  $\chi^2 = 1, 0.5$  and  $0.1$  contours.
- For a given  $r_2$ , lower  $1 - \sigma$  of  $\Delta\Theta_{obs}$  requires a smaller  $\alpha_3$  compared to upper  $1 - \sigma$  value of  $\Delta\Theta_{obs}$  (refer Figures 17a to 17d).
- Black hole with larger dilaton charge requires denser homogeneous plasma environment to explain the data.
- For any given  $r_2$  we always have some  $\alpha_3$  (where  $0 \leq \alpha_3 \leq 1$ ) which can explain the data. Hence, for homogeneous plasma we cannot rule out any parameter space of  $r_2$  and  $\alpha_3$ .
- The above observations are true for mass and distance measurements reported by the Keck and GRAVITY collaboration.

## 6 Conclusion

In this work, we have studied the influence of plasma on the shadow characteristics of the Kerr-Sen black hole, a black hole solution [39] derived from Einstein-Maxwell Dilaton-Axion (EMDA) gravity. By considering different plasma profiles, we derived constraints on the dilaton charge and plasma parameters which enable us to understand the interplay between the background metric and the plasma environment in explaining the observed images of M87\* [4] and Sgr A\* [11]. Astrophysical black holes are not isolated systems and are in general surrounded by accretion disks consisting of plasma. Thus, the present work is a continuation of our previous work [46] where the effect of plasma was not considered. Further, this would also contribute to the understanding of black hole properties in alternative gravity models. We have calculated the equations describing the shape of the shadow of a Kerr Sen black hole surrounded by non-magnetized, pressure-

less plasma and studied the variation of the shadow with dilaton charge  $r_2$ , plasma parameter  $\alpha_i$  ( $i = 1, 2, 3$  for profile 1, 2 and 3 respectively), spin  $a$  and angle of inclination  $\theta_i$ . We observed that:

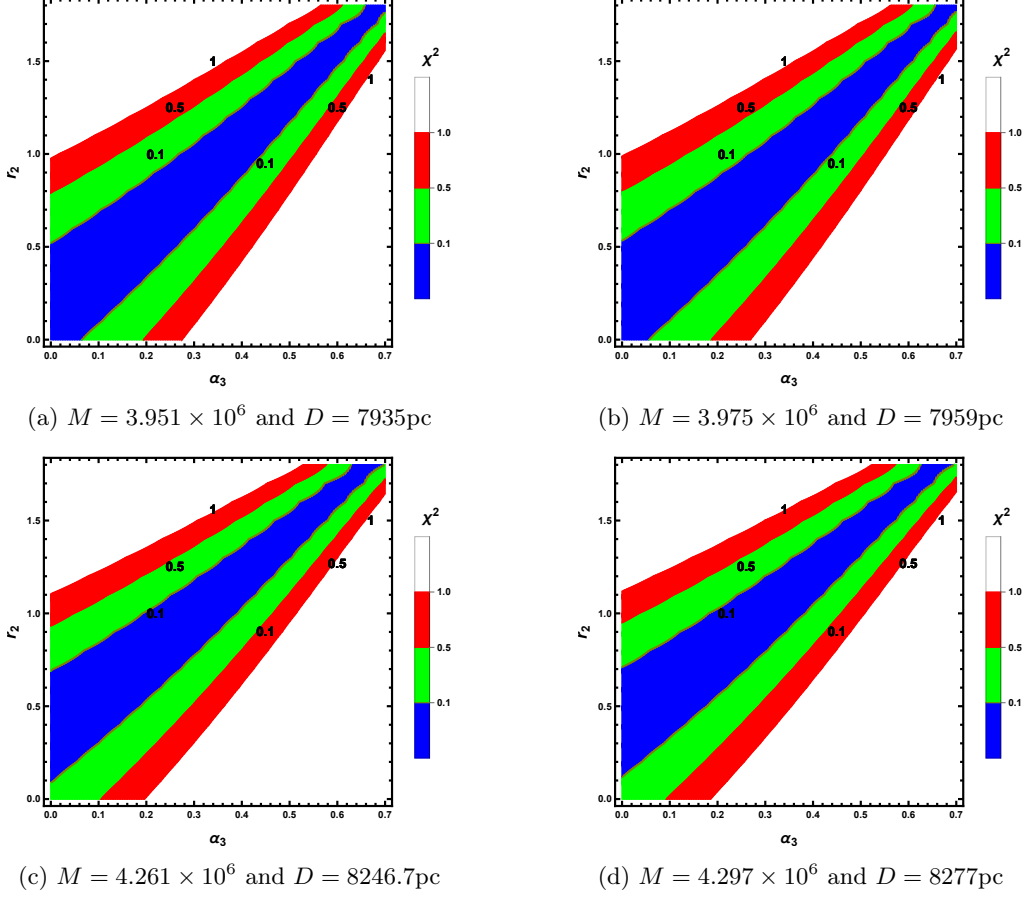


Figure 17: The figures represent contour plots of  $\chi^2$  (calculated using Equation (80) corresponding to  $a_{min}$ ) for Keck and GRAVITY collaboration mass and distance measurements for Sgr A\* surrounded by plasma profile 3. In the figures, the red color region of  $\alpha_1 - r_2$  plane corresponds to  $0.5 \leq \chi^2 \leq 1$ , the region with  $0.1 \leq \chi^2 \leq 0.5$  is colored green and the blue region represents  $0 \leq \chi^2 \leq 0.1$ . For all figures the angle of inclination  $\theta_i = 46^\circ$ .

- With increase in the dilaton charge  $r_2$  the shadow size decreases irrespective of the spin  $a$  of the black hole, the angle of inclination of the observer  $\theta_i$  and the plasma environment considered. This indicates that the contracting effect of  $r_2$  on the shadow size is generic.
- The distortion of the shadow from its circular shape increases as both the spin  $a$  and inclination angle  $\theta_i$  are increased. The shift in the geometric center of the shadow increases with increase in the spin  $a$ .
- The increase in plasma parameters  $\alpha_1$  (for profile 1 represented by Equation (73)) and  $\alpha_2$  (for

profile 2 represented by Equation (74)) decrease the shadow size irrespective of the choice of  $r_2$ ,  $a$  and  $\theta_i$ . Thus, the non-homogeneous plasma environments have a contracting effect on the shadow.

- However, the degree of contraction of the shadow size due to the plasma profiles 1 and 2 depend on the mass  $M$  and the distance  $D$  of the black hole from the observer.
- Furthermore, as the plasma parameters ( $\alpha_1$  and  $\alpha_2$ ) were increased the shape of the shadow became more circular even for high spin  $a$  and inclination angle  $\theta_i$  but the shift in geometric center persisted. This indicates that the distortion of the shadow from circular shape lessens in presence of plasma, i.e. inhomogeneous plasma environments may obliterate the effects of high spin and inclination.
- A light ray propagating in the Kerr Sen spacetime can reach an observer only when plasma parameters  $\alpha_1$  and  $\alpha_2$  are less than a certain upper bound. These bounds, which are directly related to the density of the plasma (refer Section 4), strongly depend on the dilaton charge of the Kerr Sen black hole (refer Sections 4.1 and 4.2). As  $r_2$  increases, the upper bounds on both  $\alpha_1$  and  $\alpha_2$  decrease (refer Figures 1 and 5). Thus Kerr Sen black holes surrounded by plasma environments with density above the corresponding theoretical upper bounds may not be detectable by electromagnetic observations.
- The homogeneous plasma (plasma profile 3 represented by Equation (75)) on the other hand, has an expanding effect on the shadow size and unlike the inhomogeneous plasma environments, the shadow continues to be non-circular due to the combined effect of spin  $a$  and inclination  $\theta_i$  in the presence of moderately dense homogeneous plasma environments.

In order to decipher the observationally favored dilaton charge and plasma parameters we have used the EHT observations related to the shadows of M87\* and Sgr A\*. The EHT collaboration reported the angular diameter of the primary ring of M87\* to be  $(42 \pm 3)\mu as$  with a maximum offset of 10% between the primary ring and the shadow [5]. We have taken into account the maximum offset, thus the shadow angular diameter of M87\* is taken to be  $\Delta\Theta_{obs} = (37.8 \pm 3)\mu as$ . For Sgr A\*, the EHT collaboration reported the angular diameter of the shadow to be  $\Delta\Theta_{obs} = (48.7 \pm 7)\mu as$ . We have used the methodology described in Section 5 to obtain the constraints. We have used previously reported mass  $M$ , distance  $D$  and inclination angle  $\theta_i$  measurements for M87\* and Sgr A\* to calculate their theoretical angular diameter.

For M87\* the distance  $D = 16.8\text{Mpc}$  [98, 99, 117], inclination angle  $\theta_i = 17^\circ$  [100] and mass estimates from gas dynamics studies [4, 97], and stellar dynamics studies [4, 95, 96] are used to calculate the theoretical shadow angular diameter  $\Delta\Theta_{th}$ . For purpose of completeness and comparison, we also constrained the dilaton charge and the plasma parameter using the mass estimated by the EHT team [4, 5]. We report the following important results:

- The allowed range of dilaton charge within the observed  $1 - \sigma$  interval depends on the plasma environment. In the case of non-homogeneous plasma (which are also more realistic), as the plasma density is increased (i.e.,  $\alpha_1$  and  $\alpha_2$  are enhanced in the allowed range), the corresponding upper bounds of  $r_2$  required to reproduce the observed image of M87\* within  $1 - \sigma$  decreases. This is due to the contracting effect of the shadow size due to  $\alpha_1$ ,  $\alpha_2$  and  $r_2$ .
- However, the presence of homogeneous plasma (which has an expanding effect on shadow size) enhances the upper bounds of  $r_2$  such that the observed shadow is reproduced. When



homogeneous plasma is considered, we find that the entire allowed range of  $\alpha_3$ , (i.e.,  $0 \leq \alpha_3 \leq 1$ ) lies within the observed  $1 - \sigma$ , hence no constraints are obtained.

- For the non-homogeneous profiles 1 and 2 when mass estimate of M87\* from gas dynamics studies ( $M \sim 3.5 \times 10^9 M_\odot$ ) is used to calculate  $\Delta\Theta_{th}$ , the observed angular diameter  $\Delta\Theta_{obs}$  of M87\* could not be reproduced even within  $1 - \sigma$  for any combination of  $r_2$ ,  $a$ ,  $\alpha_1$  and  $\alpha_2$ . This is consistent with our previous work [46] where the effects of plasma were not taken into account. However, with homogeneous plasma  $\Delta\Theta_{obs}$  can be reproduced if  $\alpha_3 \gtrsim 0.72$  is considered. Thus, the observed shadow of M87\* rules out homogeneous plasma parameter  $\alpha_3 \lesssim 0.72$  while inhomogeneous plasma environments rule out  $M \sim 3.5 \times 10^9 M_\odot$  which is also inconsistent with the mass estimate of M87\* by the EHT team, i.e.,  $M = 6.5 \pm 0.7 \times 10^9 M_\odot$ .
- When the mass of M87\* based on stellar dynamics studies ( $M = 6.2 \times 10^9 M_\odot$ ) is used to calculate  $\Delta\Theta_{th}$ , we observe that  $r_2 > 0.48$  fails to reproduce the image of M87\* within the observed  $1 - \sigma$ , irrespective of the inhomogeneous plasma environment considered. Further, the shadow of M87\* rules out  $\alpha_1 > 2.5$  and  $\alpha_2 > 3.8$ . The lowest value of  $\chi^2$  considering plasma profile 1 is obtained for  $\alpha_1 \sim 0.1$ ,  $r_2 \sim 0$  and  $a \sim 0.2$ . When plasma profile 2 is considered  $\alpha_2 \sim 0.2$ ,  $r_2 \sim 0$  and  $a \sim 0.1$  minimizes the  $\chi^2$ . Thus, the Kerr scenario is more favored by the EHT observations of M87\* for both the inhomogeneous plasma profiles considered here, in agreement with our previous work [46]. The silhouette of M87\* fails to constrain its dilaton charge if a homogeneous plasma environment is considered.
- The allowed spin range for M87\* using the stellar dynamics mass estimate within the observed  $1 - \sigma$  interval is found to be  $0 \lesssim a \lesssim 0.3$ . The spin constraint is the nearly the same for both the inhomogeneous plasma profiles. The previously reported spin estimates of M87\* [100, 107] are higher than the bounds obtained here which may be due to the weak dependence of angular diameter of the shadow on the spin at low inclination angles (which for M87\* is  $\theta_i \approx 17^\circ$ ) [107–109].

Next we summarize our constraints on the dilaton charge  $r_2$  and the plasma parameters using the EHT observations of Sgr A\*. In case of Sgr A\* also, we used previously reported measurements of mass, distance and inclination angle to calculate the theoretical angular diameter  $\Delta\Theta_{th}$  of the shadow. The inclination angle  $\theta_i \approx 46^\circ$  [104] while the mass and distance estimates are provided by the Keck team and the GRAVITY collaboration.

- For the two sets of Keck collaboration mass and distance measurements, the constraints on the dilaton charge and the plasma environment obtained are nearly the same because the two sets of mass and distance measurements are not very different. When  $\Delta\Theta_{th}$  is calculated with the aforesaid mass and distance estimates, we find that  $r_2 > 1$  is ruled out outside the observed  $1 - \sigma$  interval irrespective of the inhomogeneous plasma environment considered. Further, the shadow of Sgr A\* disfavors  $\alpha_1 > 5.2$  and  $\alpha_2 > 4.4$ .
- When the mass and distance reported by the Keck collaboration that fixes the redshift parameter to unity is used to calculate  $\Delta\Theta_{th}$ ,  $\alpha_1 \sim 0.3$ ,  $r_2 \sim 0.2$  and  $a \sim 0.45$  minimizes the  $\chi^2$  for plasma profile 1 while  $\alpha_2 \sim 0.4$ ,  $r_2 \sim 0.1$  and  $a \sim 0.76$  minimizes the  $\chi^2$  for plasma profile 2, indicating a marginal preference towards the EMDA scenario. When mass and distance reported by the Keck team by keeping redshift parameter free is considered, the lowest value of  $\chi^2$  is obtained for  $\alpha_1 \sim 1.2$ ,  $r_2 \sim 0$  and  $a \sim 0.7$  (for profile 1) while  $\alpha_2 \sim 1.3$ ,  $r_2 \sim 0$  and

$a \sim 0.3$  minimizes the  $\chi^2$  (for plasma profile 2), thereby favoring the Kerr scenario. Thus, either GR or Kerr-Sen black holes with mild dilaton charges is favored.

- When the two sets of mass and distance measurements of Sgr A\* by the GRAVITY collaboration are considered to calculate  $\Delta\Theta_{th}$ ,  $r_2 > 1.1$  is ruled out outside  $1 - \sigma$  irrespective of the choice of the inhomogeneous plasma environments, while  $\alpha_1 > 6$  and  $\alpha_2 > 5.2$  are ruled out by the image of Sgr A\*.
- When  $\Delta\Theta_{th}$  is calculated using mass and distance estimates of Sgr A\* by the GRAVITY collaboration without considering optical aberration,  $\alpha_1 \sim 0.9$ ,  $r_2 \sim 0.2$  and  $a \sim 0.81$  minimizes the  $\chi^2$  (for plasma profile 1) while  $\alpha_2 \sim 1.2$ ,  $r_2 \sim 0.2$  and  $a \sim 0.27$  minimizes the  $\chi^2$  (for plasma profile 2). When mass and distance assuming optical aberration is considered, the lowest value of  $\chi^2$  is obtained for  $\alpha_1 \sim 1.6$ ,  $r_2 \sim 0.2$  and  $a \sim 0.27$  for profile 1 and  $\alpha_2 \sim 0$ ,  $r_2 \sim 0.5$  and  $a \sim 0.075$  for profile 2. Thus, in this case the EMDA scenario is favored compared to GR, although the Kerr scenario is allowed within  $1-\sigma$  and this result holds good for both the inhomogeneous plasma environments.
- The present analysis could not constrain the spin of Sgr A\*. Interestingly, previous estimates assuming Sgr A\* to be a Kerr BH yield diverse results covering the entire allowed range [110–116] which are often not mutually consistent. This probably indicates revisiting the spin estimate of Sgr A\*.

The above discussion elucidates that even with the present precision of the data, shadow related observations rule out very large values of dilaton charge for M87\* and Sgr A\* in presence of inhomogeneous plasma environments (which seem to be more realistic). The presence of plasma further constrains the allowed parameter space of  $r_2$ . Furthermore, the shadow of M87\* and Sgr A\* rule out very dense inhomogeneous plasma environments surrounding these objects. While the shadow of M87\* marginally favors the Kerr scenario, the shadow of Sgr A\* exhibits a slight preference towards the Kerr-Sen scenario. In any case, within the observed  $1-\sigma$  interval, the present data cannot distinguish between the Kerr and the Kerr-Sen black holes with mild dilaton charges. In this regard, it may be worthwhile to mention that the shadow provides a cleaner probe to the background spacetime compared to other electromagnetic observations, e.g. the continuum spectrum or the Fe-line, which has been further supported by the persistent shadow of M87\* reported by the EHT team [106]. Hence, the finding that BHs with large dilaton charges are disfavored by shadow related observations seem to be quite robust. The present findings are consistent with earlier results from observations related to the continuum spectrum [47], the quasi-periodic oscillations [49] and the observed jet-power [50], although using different BH samples. Shadow related observations fail to provide strong constraints on the spin of M87\* and Sgr A\*, which may be attributed to the low inclination angle of these objects. These findings not only underscore the importance of considering plasma effects in shadow related studies but also provide a pathway for refining constraints on alternative gravitational theories using black hole observations. With the availability of more precise data, the error bars on the observed angular diameters are expected to reduce which in turn will enable us to establish stronger constraints on the background spacetime as well as the surrounding plasma environment.

## References

- [1] **LIGO Scientific, Virgo** Collaboration, B. P. Abbott *et al.*, “Observation of Gravitational Waves from a Binary Black Hole Merger,” *Phys. Rev. Lett.* **116** no. 6, (2016) 061102, [arXiv:1602.03837 \[gr-qc\]](#).
- [2] **LIGO Scientific, Virgo** Collaboration, B. P. Abbott *et al.*, “GW170817: Observation of Gravitational Waves from a Binary Neutron Star Inspiral,” *Phys. Rev. Lett.* **119** no. 16, (2017) 161101, [arXiv:1710.05832 \[gr-qc\]](#).
- [3] **LIGO Scientific, Virgo** Collaboration, B. P. Abbott *et al.*, “GWTC-1: A Gravitational-Wave Transient Catalog of Compact Binary Mergers Observed by LIGO and Virgo during the First and Second Observing Runs,” *Phys. Rev. X* **9** no. 3, (2019) 031040, [arXiv:1811.12907 \[astro-ph.HE\]](#).
- [4] **Event Horizon Telescope** Collaboration, K. Akiyama *et al.*, “First M87 Event Horizon Telescope Results. I. The Shadow of the Supermassive Black Hole,” *Astrophys. J. Lett.* **875** (2019) L1, [arXiv:1906.11238 \[astro-ph.GA\]](#).
- [5] **Event Horizon Telescope** Collaboration, K. Akiyama *et al.*, “First M87 Event Horizon Telescope Results. VI. The Shadow and Mass of the Central Black Hole,” *Astrophys. J. Lett.* **875** no. 1, (2019) L6, [arXiv:1906.11243 \[astro-ph.GA\]](#).
- [6] **Event Horizon Telescope** Collaboration, K. Akiyama *et al.*, “First M87 Event Horizon Telescope Results. III. Data Processing and Calibration,” *Astrophys. J. Lett.* **875** no. 1, (2019) L3, [arXiv:1906.11240 \[astro-ph.GA\]](#).
- [7] **Event Horizon Telescope** Collaboration, K. Akiyama *et al.*, “First M87 Event Horizon Telescope Results. V. Physical Origin of the Asymmetric Ring,” *Astrophys. J. Lett.* **875** no. 1, (2019) L5, [arXiv:1906.11242 \[astro-ph.GA\]](#).
- [8] **Event Horizon Telescope** Collaboration, K. Akiyama *et al.*, “First M87 Event Horizon Telescope Results. IV. Imaging the Central Supermassive Black Hole,” *Astrophys. J. Lett.* **875** no. 1, (2019) L4, [arXiv:1906.11241 \[astro-ph.GA\]](#).
- [9] **Event Horizon Telescope** Collaboration, K. Akiyama *et al.*, “First M87 Event Horizon Telescope Results. II. Array and Instrumentation,” *Astrophys. J. Lett.* **875** no. 1, (2019) L2, [arXiv:1906.11239 \[astro-ph.IM\]](#).
- [10] **Event Horizon Telescope** Collaboration, P. Kocherlakota *et al.*, “Constraints on black-hole charges with the 2017 EHT observations of M87\*,” *Phys. Rev. D* **103** no. 10, (2021) 104047, [arXiv:2105.09343 \[gr-qc\]](#).
- [11] **EveMartin J. Comptes Rendus Physique 13:566 (2012)nt Horizon Telescope** Collaboration, K. Akiyama *et al.*, “First Sagittarius A\* Event Horizon Telescope Results. II. EHT and Multiwavelength Observations, Data Processing, and Calibration,” *Astrophys. J. Lett.* **930** no. 2, (2022) L13.
- [12] **Event Horizon Telescope** Collaboration, K. Akiyama *et al.*, “First Sagittarius A\* Event Horizon Telescope Results. IV. Variability, Morphology, and Black Hole Mass,” *Astrophys. J. Lett.* **930** no. 2, (2022) L15.

- [13] **Event Horizon Telescope** Collaboration, K. Akiyama *et al.*, “First Sagittarius A\* Event Horizon Telescope Results. V. Testing Astrophysical Models of the Galactic Center Black Hole,” *Astrophys. J. Lett.* **930** no. 2, (2022) L16.
- [14] **Event Horizon Telescope** Collaboration, K. Akiyama *et al.*, “First Sagittarius A\* Event Horizon Telescope Results. I. The Shadow of the Supermassive Black Hole in the Center of the Milky Way,” *Astrophys. J. Lett.* **930** no. 2, (2022) L12.
- [15] **Event Horizon Telescope** Collaboration, K. Akiyama *et al.*, “First Sagittarius A\* Event Horizon Telescope Results. III. Imaging of the Galactic Center Supermassive Black Hole,” *Astrophys. J. Lett.* **930** no. 2, (2022) L14.
- [16] **Event Horizon Telescope** Collaboration, K. Akiyama *et al.*, “First Sagittarius A\* Event Horizon Telescope Results. VI. Testing the Black Hole Metric,” *Astrophys. J. Lett.* **930** no. 2, (2022) L17.
- [17] C. M. Will, “The Confrontation between General Relativity and Experiment,” *Living Rev. Rel.* **17** (2014) 4, [arXiv:1403.7377 \[gr-qc\]](#).
- [18] M. Wright, J. Janquart, and N. K. Johnson-McDaniel, “Effect of Deviations from General Relativity on Searches for Gravitational-wave Microlensing and Type II Strong Lensing,” *Astrophys. J.* **981** no. 2, (2025) 133, [arXiv:2403.08957 \[gr-qc\]](#).
- [19] **LIGO Scientific, Virgo** Collaboration, B. P. Abbott *et al.*, “Tests of general relativity with GW150914,” *Phys. Rev. Lett.* **116** no. 22, (2016) 221101, [arXiv:1602.03841 \[gr-qc\]](#). [Erratum: *Phys.Rev.Lett.* 121, 129902 (2018)].
- [20] E. Berti *et al.*, “Testing General Relativity with Present and Future Astrophysical Observations,” *Class. Quant. Grav.* **32** (2015) 243001, [arXiv:1501.07274 \[gr-qc\]](#).
- [21] J. Martin, “Everything You Always Wanted To Know About The Cosmological Constant Problem (But Were Afraid To Ask),” *Comptes Rendus Physique* **13** (2012) 566–665, [arXiv:1205.3365 \[astro-ph.CO\]](#).
- [22] S. Weinberg, “The Cosmological Constant Problem,” *Rev. Mod. Phys.* **61** (1989) 1–23.
- [23] **Supernova Search Team** Collaboration, A. G. Riess *et al.*, “Observational evidence from supernovae for an accelerating universe and a cosmological constant,” *Astron. J.* **116** (1998) 1009–1038, [arXiv:astro-ph/9805201](#).
- [24] **Supernova Cosmology Project** Collaboration, S. Perlmutter *et al.*, “Measurements of  $\Omega$  and  $\Lambda$  from 42 high redshift supernovae,” *Astrophys. J.* **517** (1999) 565–586, [arXiv:astro-ph/9812133](#).
- [25] R. Penrose, “Gravitational collapse and space-time singularities,” *Phys. Rev. Lett.* **14** (1965) 57–59.
- [26] S. W. Hawking and R. Penrose, “The Singularities of gravitational collapse and cosmology,” *Proc. Roy. Soc. Lond. A* **314** (1970) 529–548.
- [27] S. W. Hawking, “Singularities in the universe,” *Phys. Rev. Lett.* **17** (1966) 444–445.

- [28] D. N. Page, “Hawking radiation and black hole thermodynamics,” *New J. Phys.* **7** (2005) 203, [arXiv:hep-th/0409024](#).
- [29] C. Bambi, *Black Holes: A Laboratory for Testing Strong Gravity*. Springer, 2017.
- [30] S. E. Gralla, D. E. Holz, and R. M. Wald, “Black Hole Shadows, Photon Rings, and Lensing Rings,” *Phys. Rev. D* **100** no. 2, (2019) 024018, [arXiv:1906.00873 \[astro-ph.HE\]](#).
- [31] E. Teo, “Spherical Photon Orbits Around a Kerr Black Hole,” *Gen. Rel. Grav.* **35** no. 11, (2003) 1909–1926.
- [32] V. Perlick, *Ray optics, Fermat’s principle, and applications to general relativity*, vol. 61. Springer Science & Business Media, 2000.
- [33] V. Perlick, “Gravitational lensing from a spacetime perspective,” *Living Rev. Rel.* **7** (2004) 9. [10.12942/lrr-2004-9](#).
- [34] J. L. Synge, “The Escape of Photons from Gravitationally Intense Stars,” *Mon. Not. Roy. Astron. Soc.* **131** no. 3, (1966) 463–466.
- [35] J. M. Bardeen, “Properties of Black Holes Relevant to Their Observation (invited Paper),” in *Gravitational Radiation and Gravitational Collapse*, C. Dewitt-Morette, ed., vol. 64 of *IAU Symposium*, p. 132. Jan., 1974.
- [36] V. Perlick, O. Y. Tsupko, and G. S. Bisnovatyi-Kogan, “Influence of a plasma on the shadow of a spherically symmetric black hole,” *Phys. Rev. D* **92** no. 10, (2015) 104031, [arXiv:1507.04217 \[gr-qc\]](#).
- [37] V. Perlick and O. Y. Tsupko, “Light propagation in a plasma on Kerr spacetime: Separation of the Hamilton-Jacobi equation and calculation of the shadow,” *Phys. Rev. D* **95** no. 10, (2017) 104003, [arXiv:1702.08768 \[gr-qc\]](#).
- [38] M. Rogatko, “Positivity of energy in Einstein-Maxwell axion dilaton gravity,” *Class. Quant. Grav.* **19** (2002) 5063–5072, [arXiv:hep-th/0209126](#).
- [39] A. Sen, “Rotating charged black hole solution in heterotic string theory,” *Phys. Rev. Lett.* **69** (1992) 1006–1009, [arXiv:hep-th/9204046](#).
- [40] G. N. Gyulchev and S. S. Yazadjiev, “Kerr-Sen dilaton-axion black hole lensing in the strong deflection limit,” *Phys. Rev. D* **75** (2007) 023006, [arXiv:gr-qc/0611110](#).
- [41] J. An, J. Peng, Y. Liu, and X.-H. Feng, “Kerr-Sen Black Hole as Accelerator for Spinning Particles,” *Phys. Rev. D* **97** no. 2, (2018) 024003, [arXiv:1710.08630 \[gr-qc\]](#).
- [42] Z. Younsi, A. Zhidenko, L. Rezzolla, R. Konoplya, and Y. Mizuno, “New method for shadow calculations: Application to parametrized axisymmetric black holes,” *Phys. Rev. D* **94** no. 8, (2016) 084025, [arXiv:1607.05767 \[gr-qc\]](#).
- [43] K. Hioki and U. Miyamoto, “Hidden symmetries, null geodesics, and photon capture in the Sen black hole,” *Phys. Rev. D* **78** (2008) 044007, [arXiv:0805.3146 \[gr-qc\]](#).

- [44] A. Narang, S. Mohanty, and A. Kumar, “Test of Kerr-Sen metric with black hole observations,” [arXiv:2002.12786 \[gr-qc\]](#).
- [45] S. Jana and S. Kar, “Shadows in dyonic Kerr-Sen black holes,” [arXiv:2303.14513 \[gr-qc\]](#).
- [46] S. K. Sahoo, N. Yadav, and I. Banerjee, “Imprints of Einstein-Maxwell-dilaton-axion gravity in the observed shadows of Sgr A\* and M87\*,” *Phys. Rev. D* **109** no. 4, (2024) 044008, [arXiv:2305.14870 \[gr-qc\]](#).
- [47] I. Banerjee, B. Mandal, and S. SenGupta, “Implications of Einstein–Maxwell dilaton–axion gravity from the black hole continuum spectrum,” *Mon. Not. Roy. Astron. Soc.* **500** no. 1, (2020) 481–492, [arXiv:2007.13980 \[gr-qc\]](#).
- [48] A. Tripathi, B. Zhou, A. B. Abdikamalov, D. Ayzenberg, and C. Bambi, “Constraints on Einstein-Maxwell dilaton-axion gravity from X-ray reflection spectroscopy,” *JCAP* **07** (2021) 002, [arXiv:2103.07593 \[astro-ph.HE\]](#).
- [49] A. Dasgupta, N. Tiwari, and I. Banerjee, “Signatures of Einstein-Maxwell dilaton-axion gravity from the observed quasi-periodic oscillations in black holes,” [arXiv:2503.02708 \[gr-qc\]](#).
- [50] I. Banerjee, B. Mandal, and S. SenGupta, “Signatures of Einstein-Maxwell dilaton-axion gravity from the observed jet power and the radiative efficiency,” *Phys. Rev. D* **103** no. 4, (2021) 044046, [arXiv:2007.03947 \[gr-qc\]](#).
- [51] M. A. Abramowicz and P. C. Fragile, “Foundations of Black Hole Accretion Disk Theory,” *Living Rev. Rel.* **16** (2013) 1, [arXiv:1104.5499 \[astro-ph.HE\]](#).
- [52] D. O. Muhleman and I. D. Johnston, “Radio propagation in the solar gravitational field,” *Phys. Rev. Lett.* **17** (Aug, 1966) 455–458. <https://link.aps.org/doi/10.1103/PhysRevLett.17.455>.
- [53] D. O. Muhleman, R. D. Ekers, and E. B. Fomalont, “Radio Interferometric Test of the General Relativistic Light Bending Near the Sun,” *Phys. Rev. Lett.* **24** (1970) 1377–1380.
- [54] V. Perlick, *Ray Optics, Fermat’s Principle, and Applications to General Relativity*, vol. 61. 2000.
- [55] G. S. Bisnovatyi-Kogan and O. Y. Tsupko, “Gravitational lensing in a non-uniform plasma,” *Mon. Not. Roy. Astron. Soc.* **404** (2010) 1790–1800, [arXiv:1006.2321 \[astro-ph.CO\]](#).
- [56] O. Y. Tsupko and G. S. Bisnovatyi-Kogan, “Gravitational lensing in plasma: Relativistic images at homogeneous plasma,” *Phys. Rev. D* **87** no. 12, (2013) 124009, [arXiv:1305.7032 \[astro-ph.CO\]](#).
- [57] V. S. Morozova, B. J. Ahmedov, and A. A. Tursunov, “Gravitational lensing by a rotating massive object in a plasma,” *ApSS* **346** no. 2, (Aug., 2013) 513–520.
- [58] G. Crisnejo and E. Gallo, “Weak lensing in a plasma medium and gravitational deflection of massive particles using the Gauss-Bonnet theorem. A unified treatment,” *Phys. Rev. D* **97** no. 12, (2018) 124016, [arXiv:1804.05473 \[gr-qc\]](#).



- [59] G. Crisnejo, E. Gallo, and A. Rogers, “Finite distance corrections to the light deflection in a gravitational field with a plasma medium,” *Phys. Rev. D* **99** no. 12, (2019) 124001, [arXiv:1807.00724 \[gr-qc\]](#).
- [60] G. Crisnejo, E. Gallo, and J. R. Villanueva, “Gravitational lensing in dispersive media and deflection angle of charged massive particles in terms of curvature scalars and energy-momentum tensor,” *Phys. Rev. D* **100** no. 4, (2019) 044006, [arXiv:1905.02125 \[gr-qc\]](#).
- [61] G. Crisnejo, E. Gallo, and K. Jusufi, “Higher order corrections to deflection angle of massive particles and light rays in plasma media for stationary spacetimes using the Gauss-Bonnet theorem,” *Phys. Rev. D* **100** no. 10, (2019) 104045, [arXiv:1910.02030 \[gr-qc\]](#).
- [62] C.-Q. Liu, C.-K. Ding, and J.-L. Jing, “Effects of Homogeneous Plasma on Strong Gravitational Lensing of Kerr Black Holes,” *Chin. Phys. Lett.* **34** no. 9, (2017) 090401, [arXiv:1610.02128 \[gr-qc\]](#).
- [63] A. Rogers, “Frequency-dependent effects of gravitational lensing within plasma,” *Mon. Not. Roy. Astron. Soc.* **451** no. 1, (2015) 17–25, [arXiv:1505.06790 \[gr-qc\]](#).
- [64] A. Rogers, “Escape and Trapping of Low-Frequency Gravitationally Lensed Rays by Compact Objects within Plasma,” *Mon. Not. Roy. Astron. Soc.* **465** no. 2, (2017) 2151–2159, [arXiv:1611.01269 \[gr-qc\]](#).
- [65] X. Er and S. Mao, “Effects of plasma on gravitational lensing,” *Mon. Not. Roy. Astron. Soc.* **437** no. 3, (2014) 2180–2186, [arXiv:1310.5825 \[astro-ph.CO\]](#).
- [66] P. Kumar and P. Beniamini, “Gravitational lensing in the presence of plasma scattering with application to Fast Radio Bursts,” *Mon. Not. Roy. Astron. Soc.* **520** no. 1, (2023) 247–258, [arXiv:2208.03332 \[astro-ph.HE\]](#).
- [67] G. Crisnejo, E. Gallo, E. F. Boero, and O. M. Moreschi, “Perturbative and numerical approach to plasma strong lensing,” *Phys. Rev. D* **107** no. 8, (2023) 084041, [arXiv:2212.14297 \[gr-qc\]](#).
- [68] G. S. Bisnovatyi-Kogan and O. Y. Tsupko, “Time delay induced by plasma in strong lens systems,” *Mon. Not. Roy. Astron. Soc.* **524** no. 2, (2023) 3060–3067, [arXiv:2301.00053 \[gr-qc\]](#).
- [69] O. Y. Tsupko and G. S. Bisnovatyi-Kogan, “Hills and holes in the microlensing light curve due to plasma environment around gravitational lens,” *Mon. Not. Roy. Astron. Soc.* **491** no. 4, (2020) 5636–5649, [arXiv:1910.03457 \[gr-qc\]](#).
- [70] J. Sun, X. Er, and O. Y. Tsupko, “Binary microlensing with plasma environment – star and planet,” *Mon. Not. Roy. Astron. Soc.* **520** no. 1, (2023) 994–1004, [arXiv:2211.13442 \[astro-ph.SR\]](#).
- [71] X. Er, Y.-P. Yang, and A. Rogers, “The effects of plasma lensing on the inferred dispersion measures of fast radiobursts,” *The Astrophysical Journal* **889** no. 2, (Feb, 2020) 158. <https://dx.doi.org/10.3847/1538-4357/ab66b1>.

- [72] H. Yan, “Influence of a plasma on the observational signature of a high-spin Kerr black hole,” *Phys. Rev. D* **99** no. 8, (2019) 084050, [arXiv:1903.04382 \[gr-qc\]](#).
- [73] A. Chowdhuri and A. Bhattacharyya, “Shadow analysis for rotating black holes in the presence of plasma for an expanding universe,” *Phys. Rev. D* **104** no. 6, (2021) 064039, [arXiv:2012.12914 \[gr-qc\]](#).
- [74] J. Badía and E. F. Eiroa, “Shadow of axisymmetric, stationary, and asymptotically flat black holes in the presence of plasma,” *Phys. Rev. D* **104** no. 8, (2021) 084055, [arXiv:2106.07601 \[gr-qc\]](#).
- [75] J. Badía and E. F. Eiroa, “Shadows of rotating Einstein-Maxwell-dilaton black holes surrounded by a plasma,” *Phys. Rev. D* **107** no. 12, (2023) 124028, [arXiv:2210.03081 \[gr-qc\]](#).
- [76] B. Bezdekova, V. Perlick, and J. Bicak, “Light propagation in a plasma on an axially symmetric and stationary spacetime: Separability of the Hamilton–Jacobi equation and shadow,” *J. Math. Phys.* **63** no. 9, (2022) 092501, [arXiv:2204.05593 \[gr-qc\]](#).
- [77] G. Briozzo, E. Gallo, and T. Mädler, “Shadows of rotating black holes in plasma environments with aberration effects,” *Phys. Rev. D* **107** no. 12, (2023) 124004, [arXiv:2211.05620 \[gr-qc\]](#).
- [78] V. Perlick and O. Y. Tsupko, “Light propagation in a plasma on Kerr spacetime. II. Plasma imprint on photon orbits,” *Phys. Rev. D* **109** no. 6, (2024) 064063, [arXiv:2311.10615 \[gr-qc\]](#).
- [79] D. Garfinkle, G. T. Horowitz, and A. Strominger, “Charged black holes in string theory,” *Phys. Rev. D* **43** (May, 1991) 3140–3143.  
<https://link.aps.org/doi/10.1103/PhysRevD.43.3140>.
- [80] D. Garfinkle, G. T. Horowitz, and A. Strominger, “Erratum: Charged black holes in string theory,” *Phys. Rev. D* **45** (May, 1992) 3888–3888.  
<https://link.aps.org/doi/10.1103/PhysRevD.45.3888>.
- [81] C. Ganguly and S. SenGupta, “Penrose process in a charged axion–dilaton coupled black hole,” *Eur. Phys. J. C* **76** no. 4, (2016) 213, [arXiv:1401.6826 \[hep-th\]](#).
- [82] R. H. Boyer and R. W. Lindquist, “Maximal analytic extension of the Kerr metric,” *J. Math. Phys.* **8** (1967) 265.
- [83] R. A. Breuer and J. Ehlers, “Propagation of high-frequency electromagnetic waves through a magnetized plasma in curved space-time. i,” *Proceedings of the Royal Society of London. A. Mathematical and Physical Sciences* **370** no. 1742, (1980) 389–406.
- [84] R. A. Breuer and J. Ehlers, “Propagation of high-frequency electromagnetic waves through a magnetized plasma in curved space-time. ii. application of the asymptotic approximation,” *Proceedings of the Royal Society of London. A. Mathematical and Physical Sciences* **374** no. 1756, (1981) 65–86.



- [85] J. Synge, *Relativity: The General Theory*. No. v. 1 in North-Holland series in physics. North-Holland Publishing Company, 1960.  
<https://books.google.co.in/books?id=CqoNAQAIAAJ>.
- [86] B. Carter, “Global structure of the Kerr family of gravitational fields,” *Phys. Rev.* **174** (1968) 1559–1571.
- [87] I. Banerjee, V. S. Chawan, B. Mandal, S. K. Sahoo, and S. SenGupta, “Quasar continuum spectrum disfavors black holes with a magnetic monopole charge,” *Phys. Rev. D* **105** no. 6, (2022) 064073, [arXiv:2112.05385 \[gr-qc\]](#).
- [88] A. Grenzebach, V. Perlick, and C. Lämmerzahl, “Photon Regions and Shadows of Kerr-Newman-NUT Black Holes with a Cosmological Constant,” *Phys. Rev. D* **89** no. 12, (2014) 124004, [arXiv:1403.5234 \[gr-qc\]](#).
- [89] A. Grenzebach, V. Perlick, and C. Lämmerzahl, “Photon Regions and Shadows of Accelerated Black Holes,” *Int. J. Mod. Phys. D* **24** no. 09, (2015) 1542024, [arXiv:1503.03036 \[gr-qc\]](#).
- [90] S. L. Shapiro, “Accretion onto black holes: The emergent radiation spectrum. iii. rotating (kerr) black holes,” *Astrophysical Journal*, Vol. 189, pp. 343–352 (1974) **189** (1974) 343–352.
- [91] A. Mosallanezhad, S. Abbassi, and N. Beiranvand, “Structure of advection-dominated accretion discs with outflows: the role of toroidal magnetic fields,” *Mon. Not. Roy. Astron. Soc.* **437** no. 4, (2014) 3112–3123, [arXiv:1310.6318 \[astro-ph.HE\]](#).
- [92] M. J. Rees, E. S. Phinney, M. C. Begelman, and R. D. Blandford, “Ion supported tori and the origin of radio jets,” *Nature* **295** (1982) 17–21.
- [93] S. S. Komissarov, “Magnetized Tori around Kerr Black Holes: Analytic Solutions with a Toroidal Magnetic Field,” *Mon. Not. Roy. Astron. Soc.* **368** (2006) 993–1000, [arXiv:astro-ph/0601678](#).
- [94] R. Kulsrud and A. Loeb, “Dynamics and gravitational interaction of waves in nonuniform media,” *Phys. Rev. D* **45** (1992) 525–531.
- [95] K. Gebhardt and J. Thomas, “The Black Hole Mass, Stellar M/L, and Dark Halo in M87,” *Astrophys. J.* **700** (2009) 1690–1701, [arXiv:0906.1492 \[astro-ph.CO\]](#).
- [96] K. Gebhardt *et al.*, “A Relationship between nuclear black hole mass and galaxy velocity dispersion,” *Astrophys. J. Lett.* **539** (2000) L13, [arXiv:0006013 \[astro-ph\]](#), *Comptes Rendus Physique* **13**:566 (2012) [arXiv:astro-ph/0006289](#).
- [97] J. L. Walsh, A. J. Barth, L. C. Ho, and M. Sarzi, “The M87 Black Hole Mass from Gas-dynamical Models of Space Telescope Imaging Spectrograph Observations,” *Astrophys. J.* **770** (2013) 86, [arXiv:1304.7273 \[astro-ph.CO\]](#).
- [98] J. P. Blakeslee, A. Jordan, S. Mei, P. Cote, L. Ferrarese, L. Infante, E. W. Peng, J. L. Tonry, and M. J. West, “The ACS Fornax Cluster Survey. V. Measurement and Recalibration of Surface Brightness Fluctuations and a Precise Value of the Fornax–Virgo Relative Distance,” *Astrophys. J.* **694** (2009) 556–572, [arXiv:0901.1138 \[astro-ph.CO\]](#).

- [99] S. Bird, W. E. Harris, J. P. Blakeslee, and C. Flynn, “The Inner Halo of M87: A First Direct View of the Red-Giant Population,” *Astron. Astrophys.* **524** (2010) A71, [arXiv:1009.3202 \[astro-ph.GA\]](#).
- [100] F. Tamburini, B. Thidé, and M. Della Valle, “Measurement of the spin of the M87 black hole from its observed twisted light,” *Mon. Not. Roy. Astron. Soc.* **492** no. 1, (2020) L22–L27, [arXiv:1904.07923 \[astro-ph.HE\]](#).
- [101] T. Do *et al.*, “Relativistic redshift of the star S0-2 orbiting the Galactic center supermassive black hole,” *Science* **365** no. 6454, (2019) 664–668, [arXiv:1907.10731 \[astro-ph.GA\]](#).
- [102] **GRAVITY** Collaboration, R. Abuter *et al.*, “Detection of the Schwarzschild precession in the orbit of the star S2 near the Galactic centre massive black hole,” *Astron. Astrophys.* **636** (2020) L5, [arXiv:2004.07187 \[astro-ph.GA\]](#).
- [103] **GRAVITY** Collaboration, R. Abuter *et al.*, “Mass distribution in the Galactic Center based on interferometric astrometry of multiple stellar orbits,” *Astron. Astrophys.* **657** (2022) L12, [arXiv:2112.07478 \[astro-ph.GA\]](#).
- [104] R. Abuter, A. Amorim, M. Bauböck, J. Berger, H. Bonnet, W. Brandner, Y. Clénet, V. C. Du Foresto, P. De Zeeuw, J. Dexter, *et al.*, “A geometric distance measurement to the galactic center black hole with 0.3% uncertainty,” *Astronomy & Astrophysics* **625** (2019) L10.
- [105] Y. Avni, “Energy spectra of X-ray clusters of galaxies,” *Astrophys. J.* **210** (Dec, 1976) 642–646.
- [106] **Event Horizon Telescope** Collaboration, K. Akiyama *et al.*, “The persistent shadow of the supermassive black hole of M 87. I. Observations, calibration, imaging, and analysis,” *Astron. Astrophys.* **681** (2024) A79.
- [107] R. Nemmen, “The Spin of M87\*,” *Astrophys. J. Lett.* **880** no. 2, (2019) L26, [arXiv:1905.02143 \[astro-ph.HE\]](#).
- [108] R. Takahashi, “Shapes and positions of black hole shadows in accretion disks and spin parameters of black holes,” *J. Korean Phys. Soc.* **45** (2004) S1808–S1812, [arXiv:astro-ph/0405099](#).
- [109] T. Johannsen and D. Psaltis, “Testing the No-Hair Theorem with Observations in the Electromagnetic Spectrum: II. Black-Hole Images,” *Astrophys. J.* **718** (2010) 446–454, [arXiv:1005.1931 \[astro-ph.HE\]](#).
- [110] M. Mościbrodzka, C. F. Gammie, J. C. Dolence, H. Shiokawa, and P. K. Leung, “Radiative Models of SGR A\* from GRMHD Simulations,” *Astrophys. J.* **706** no. 1, (Nov., 2009) 497–507, [arXiv:0909.5431 \[astro-ph.HE\]](#).
- [111] R. V. Shcherbakov, R. F. Penna, and J. C. McKinney, “Sagittarius A\* Accretion Flow and Black Hole Parameters from General Relativistic Dynamical and Polarized Radiative Modeling,” *Astrophys. J.* **755** no. 2, (Aug., 2012) 133, [arXiv:1007.4832 \[astro-ph.HE\]](#).

- [112] G. Fragione and A. Loeb, “An upper limit on the spin of SgrA\* based on stellar orbits in its vicinity,” *Astrophys. J. Lett.* **901** no. 2, (2020) L32, [arXiv:2008.11734 \[astro-ph.GA\]](#).
- [113] G. Belanger, R. Terrier, O. C. De Jager, A. Goldwurm, and F. Melia, “Periodic Modulations in an X-ray Flare from Sagittarius A\*,” *J. Phys. Conf. Ser.* **54** (2006) 420–426, [arXiv:astro-ph/0604337](#).
- [114] L. Meyer, A. Eckart, R. Schoedel, W. J. Duschl, K. Muzic, M. Dovciak, and V. Karas, “Near-infrared polarimetry setting constraints on the orbiting spot model for Sgr A\* flares,” *Astron. Astrophys.* **460** (2006) 15, [arXiv:astro-ph/0610104](#).
- [115] R. Genzel, R. Schodel, T. Ott, A. Eckart, T. Alexander, F. Lacombe, D. Rouan, and B. Aschenbach, “Near-infrared flares from accreting gas around the supermassive black hole at the galactic centre,” *Nature* **425** (2003) 934–937, [arXiv:astro-ph/0310821](#).
- [116] R. A. Daly, M. Donahue, C. P. O’Dea, B. Sebastian, D. Haggard, and A. Lu, “New black hole spin values for Sagittarius A\* obtained with the outflow method,” *Mon. Not. Roy. Astron. Soc.* **527** no. 1, (2023) 428–436, [arXiv:2310.12108 \[astro-ph.GA\]](#).
- [117] M. Cantiello *et al.*, “A Precise Distance to the Host Galaxy of the Binary Neutron Star Merger GW170817 Using Surface Brightness Fluctuations,” *Astrophys. J. Lett.* **854** no. 2, (2018) L31, [arXiv:1801.06080 \[astro-ph.GA\]](#).